Volcanic Emissions, Plume Dispersion and Downwind Radiative Impacts following Mount Etna Series of Eruptions of 21-26 February 2021

Pasquale Sellitto, Giuseppe Salerno, Stefano Corradini, Irène Xueref-Remy, Aurélie Riandet, Clémence Bellon, Sergey Khaykin, Gérard Ancellet, Simone Lolli, Ellsworth J. Welton, et al.

Volcanic Emissions, Plume Dispersion and Downwind Radiative Impacts following Mount Etna Series of Eruptions of 21-26 February 2021

P. Sellitto[1], G. Salerno[2], S. Corradini[3], I. Xueref-Remy[4], A. Riandet[4], C. Bellon[4], S. Khaykin[5], G. Ancellet[5], S. Lolli[6], E. J. Welton[7], A. Boselli[6], A. Sannino[8], J. Cuesta[1], H. Guermazi[1], M. Eremenko[1], L. Merucci[3], D. Stelitano[3], L. Guerrieri[3], and B. Legras[9]

[1] Univ. Paris Est Créteil and Université de Paris, CNRS, Laboratoire Interuniversitaire des Systèmes Atmosphériques, Institut Pierre Simon Laplace, Créteil, France

[2]Istituto Nazionale di Geofisica e Vulcanologia, Osservatorio Etneo, Catania, Italy.

[3]Istituto Nazionale di Geofisica e Vulcanologia, Osservatorio Nazionale Terremoti, Rome, Italy

[4]Aix Marseille Univ, Avignon Université, CNRS, IRD, Institut Méditerranéen de Biodiversité et d'Écologie marine et continentale (IMBE), Marseille, France

[5]Laboratoire Atmosphères, Milieux, Observations Spatiales, UMR CNRS 8190, IPSL, Sorbonne Univ./UVSQ, Guyancourt, France

[6]Consiglio Nazionale delle Ricerche – Istituto di Metodologie per l'Analisi Ambientale (CNR-IMAA), C. da S. Loja, Tito Scalo, Potenza, Italy

[7]NASA Goddard Space Flight Center, Code 612, Greenbelt, MD 20771, USA

[8]Dipartimento di Fisica "Ettore Pancini", Università Federico II di Napoli, Complesso Universitario di Monte S. Angelo, Via Cintia, I-80126 Napoli (Italy).

[9]Laboratoire de Météorologie Dynamique, UMR CNRS 8539, École Normale Supérieure, PSL Research University, École Polytechnique, Sorbonne Universités, École des Ponts PARISTECH, Institut Pierre Simon Laplace, Paris, France

Corresponding author: first and last name (pasquale.sellitto@lisa.ipsl.fr)

Key Points:

- Three distinct paroxysmal events took place at Mount Etna from 21 to 26 February 2021 and the plumes were transported towards the north
- Plumes dispersion is characterized with Lagrangian modelling initialized with measured SO2 emissions and with satellite observations
- A series of LiDARs detected and characterized the plumes downwind and their observations are used to estimate the plumes radiative forcing

Abstract

During the extended activity of Mount Etna volcano in February-April 2021, three distinct paroxysmal events took place from 21 to 26 February, which were associated with a very uncommon transport of the injected upper-tropospheric plumes towards the north. Using a synergy of observations and modelling, we characterised the emissions and three-dimensional dispersion for these three plumes, we monitor their downwind morphological and optical properties, and we estimate their radiative impacts at selected locations. With a satellite-based source inversion, we estimate the emitted sulphur dioxide (SO2) mass at an integrated value of 55 kt and plumes injections at up to 12 km altitudes, which combine to qualify this series as extreme in the eruption strengths spectrum for Mount Etna. We then combine Lagrangian dispersion modelling, initialised with measured temporally-resolved SO2 emission fluxes and altitudes, with satellite observations to track the dispersion of the three individual plumes. The transport towards the north allowed the height-resolved downwind monitoring of the plumes at selected observatories in France, Italy and Israel, using LiDARs and photometric aerosol observations. Volcanic-specific aerosol optical depths in the visible spectral range ranging from about 0.004 to 0.03 and local daily average shortwave radiative forcing ranging from about -0.2 to -1.2 W/m^2 (at the top of atmosphere) and from about -0.2 to -3.5 W/m^2 (at the surface) are found. Both the aerosol optical depth and the radiative forcing of the plume depends strongly on its morphology (position of the sampled section of the plume) and composition (possible presence of fine ash).

Plain Language Summary

The volcanic plumes from Mount Etna's eruptions disperse usually towards the east, to the Central-Eastern Mediterranean, where no ground stations are available to monitor and characterise them. During the extended intense volcanic activity of Mount Etna in February-April 2021, some of the plumes dispersed towards the north, in an area where many and well-equipped ground observatories are available. This was a unique and very uncommon possibility to study the emissions, dispersion dynamics, shape/composition and impacts of Mount Etna's emissions. We analysed these rare events using all available information layers: satellite observations, numerical simulation of the plume's dispersion and downwind ground-based observatories. By coupling these information pieces, we could reconstruct these events and untangle their impacts from those of a major Saharan dust outbreak that occurred simultaneously. These events were found quite extreme for the Mediterranean volcanism (extreme emissions and at altitudes as high as 12 km). We found that this kind of volcanic eruptions have a relevant (and not yet studied) impact on the upper-tropospheric composition and regional climate in the Mediterranean area. The plumes, after regional-to-continental dispersion, exhibit a complex filamentary morphology and, and most likely, a complex composition coming from the interplay of sulphur compounds and ash emissions.

1 Introduction

Volcanic activity, spanning from passive degassing to explosive eruptions, can have relevant downwind impacts on the atmospheric composition (e.g. von Glasow et al., 2009), aerosol properties (e.g. Sellitto et al., 2017), air quality and health (e.g. Michaud et al., 2005), the formation and lifetime of clouds (e.g. Malavelle et al., 2017) and the radiative balance (e.g. Andersson et al., 2015, Sellitto et al., 2020, Kloss et al., 2021). Associated with the volcanic activity are both primary emissions of gases and particles, like water vapour, carbon dioxide, sulphur dioxide (SO2) and ash, and secondary aerosols, in particular the tiny-sized sulphate aerosols (SA) forming from

the gaseous- and liquid-phase oxidation/nucleation from SO2 primary emissions. All these effluents can have environmental and climatic impacts downwind the dispersion pathways of the volcanic plumes. The SA, in particular, are the main contributors of the volcanogenic modulation of the Earth's radiative balance and, then, of the local, regional or global climate system (Sellitto and Briole, 2015). This is due to their high reflectivity properties in the solar spectral range, mirrored by their very high single scattering albedo (SSA) (Krotkov at al., 1997), and their relatively long atmospheric residence time, linked to their tiny typical sizes (Stevenson et al., 2003). While the importance of moderate-to-strong volcanic eruptions, with plume injection in the stratosphere, on the Earth's climate system is now relatively well established (Santer et al., 2014; Ridley et al., 2017), the role on the regional climate system of smaller eruptions, with injection in the troposphere, as well as local impacts of persistent passive degassing activity (Sellitto et al., 2020), is not yet well understood and quantified (Oppenheimer et al., 2011).

The downwind impacts of tropospheric volcanic plumes and their spatio-temporal extent depend critically on the interplay of three main aspects: 1) the internal geochemical and geophysical processes linked to magma degassing and plume injection, and, once the plume is released, 2) its atmospheric physico-chemical evolution, and 3) the local and regional atmospheric dynamics driving the plume dispersion. To characterise these three components of the plumes release and evolution, as well as to estimate downwind impacts, a coordinated synergy of ground-based and satellite observations, and the modelling of transport and physical-chemical evolution, are necessary. Such synergies have been exploited in a number of studies in the past (e.g. Haywood et al., 2010; Webley et al., 2012; Sellitto et al., 2016; Kloss et al., 2021).

In this paper, we couple ground-based and satellite observations with dispersion and impact modelling to study a specific phase of the extended activity of Mount Etna occurring during the period February-April 2021. We focus, in particular, on the series of paroxysmal eruptions during the period from 21 to 26/02/2021. This period was characterized by an uncommon local dynamics that allowed a rare transport of the emitted plumes towards the north, where a number of ground-based observatories could be used to monitor the morphological, optical and radiative properties of the plumes. Vertically-resolved information can be retrieved from stations equipped with LiDAR (Light Detection And Ranging) systems. From several points of view, this is a unique case-study to gather better insights into the evolution of a moderate volcanic eruption: the extended period of the activity, the unusual intensity of the eruptions, the relatively high altitude of the atmospheric injection and the transport towards areas with a relatively large density of potential downwind observations. Here we show that, in such conditions, a synergistic observational/modelling approach can contribute a more complete end-to-end characterisation of the volcanic events, from emissions to dispersion to downwind impacts.

The paper is organized as follows. In Sect. 2 we introduce and describe the array of observations and modelling tools used in this work. In Sect. 3 we provide a qualitative description of the eruptive series under investigation, and we frame this volcanic activity into the wider Mount Etna's internal geophysical context. In Sect. 4 we show results for the characterisation of the emission, dispersion and impacts of this series of events. We draw conclusions in Sect. 5.

2 Data and Methods

2.1 Volcanic SO2 emission flux rates and total mass estimations from satellite-based source inversion

The SO2 emission flux rates time series and total mass have been obtained by exploiting the measurements collected from the Spinning Enhanced Visible and InfraRed Imager (SEVIRI). The SEVIRI instrument is a multispectral imager on board the Meteosat Second Generation (MSG) geostationary satellite. It has 12 spectral channels from visible to Thermal InfraRed (TIR) spectral ranges and a spatial resolution of 3 km at sub-satellite point. The temporal resolution varies from 5 (rapid scan mode over Europe and Northern Africa) to 15 min (Earth full disk) (see https://www.eumetsat.int/meteosat-second-generation for more details on MSG platform and SEVIRI instrument). The SEVIRI measurements are collected in real time from the Multimission Acquisition SysTem (MAST) developed at Istituto Nazionale di Geofisica e Vulcanologia (INGV) (Stelitano et al., 2020). All the SEVIRI images used in this work have been resampled in a regular grid of 3×3 km^2 and processed every 15 minutes.

The SO2 columnar abundance is computed by applying the Volcanic Plume Retrieval (VPR) procedure (Guerrieri et al., 2015). This approach is based on the computations of the plume transmittances in the SEVIRI TIR bands centred at 8.7, 10.8, and 12 μm, obtained through linear equations based on the original image radiances and a new image with volcanic plume signal removed; the latter is computed by means of a linear regression of the radiance values outside the edges of the plume itself. The SO2 estimates are obtained from 8.7 μm transmittances, after eliminating the contribution of ash and ice particles computed from 10.8 and 12 μm channels. The main advantage of VPR is that the only input required is the volcanic cloud top height.

From the SO2 abundance, the SO2 emission flux rate is obtained by applying the "traverse approach" (Corradini et al., 2008; Merucci et al., 2011) considering a transect placed at 30±1.5 km from the summit craters and a wind speed derived from the ARPA (Agenzia Regionale per la Protezione Ambientale) database (Scollo et al., 2009). Such a distance for the reference transect has been selected to minimize the retrieval uncertainties induced by both the opacity of the pixels too close to the craters and the dilution of the pixels too far from the emission. Knowing the wind speed, the SO2 flux at 30 km is then reported to 0 km over the vents (Corradini et al., 2020; 2021). From SO2 emission rate, the SO2 total emitted mass is obtained by temporal integration.

The volcanic cloud top height is obtained by applying the consolidated "dark pixel" procedure (Prata et al., 2001; Scollo et al., 2014; Corradini et al., 2018) , based on the comparison between the minimum SEVIRI 10.8 μm brightness temperature of a pixel contained in a fixed area over the summit craters and an atmospheric temperature profile measured approximately in the same area and at the same time of satellite acquisition (Scollo et al., 2014; Corradini et al., 2018). In this case an area of 19x19 SEVIRI pixels and ARPA database were used respectively. This method is based on the assumption that the plume is opaque and in thermal equilibrium with its environment.

2.2 Model simulations of plume dispersion and impacts

2.2.1 Plume dispersion with the FLEXPART Lagrangian model

We simulate the dispersion of the SO2 plumes emanated by the Mount Etna activity during the period 21-26/02/2021 using the Lagrangian dispersion model FLEXPART (Pisso et al., 2019). The simulations are initialized with the emission rates and altitude estimated with SEVIRI, using the methods described in Sect. 2.1. As meteorological inputs, our FLEXPART simulations use

European Centre for Medium-Range Weather Forecasts (ECMWF) ERA-5 reanalysis data at 30 km horizontal resolution and 137 height levels (100–200 m vertical resolution in the troposphere, 1–2 km in the lower stratosphere). The FLEXPART outputs are averaged over 30 min intervals and are given at 0.1° x 0.1° horizontal grid and 9 altitude levels, from the surface to 13 km altitude, with a vertical resolution of 1 km, from 5 to 13 km, and a unique vertically-broad layer, from surface to 5 km. Dry and wet deposition, as well as chemical depletion, are considered in the simulations, using the default FLEXPART sink parameterization for SO2.

2.2.2 Plume radiative forcing estimations with the UVSPEC radiative transfer model

We estimate the radiative impact of the Mount Etna plumes for the events under investigation using the radiative transfer model UVSPEC and the LibRadtran package (Emde et al., 2016). The equinox-equivalent clear-sky daily-average shortwave (integrated between 300 and 3000 nm) surface and top of the atmosphere (TOA) direct radiative forcings (RF) are estimated with a similar methodology as done by Sellitto et al. (2016, 2020); please refer to these previous works for more details on the setup of the radiative model.
The background atmospheric state is set using the AFGL (Air Force Geophysics Laboratory) winter mid-latitudes climatological standard. The surface albedo is set to 0.15, independent from wavelength, which is a typical average shortwave albedo for the vegetated surfaces underlying the locations associated with our study. Baseline and volcanically-perturbed radiative transfer calculations are carried out using different aerosol layers configurations: using aerosol extinction profiles at downwind LiDAR stations, as volcanically-perturbed conditions, and with the same aerosol extinction profiles with the identified volcanic plume layer removed, as non-volcanic baseline (see specific configurations in Sec. 4.5). Different hypotheses must be considered for the non-measured optical parameters of volcanic aerosols. The spectral variability of the volcanic aerosol extinction, the single scattering albedo and the angular distribution of the scattered radiation are not directly measured and can be quite uncertain due to the possible presence of both SA and a fraction of residual ash. Values of the Ångström exponent (a compact measure of the spectral variability of the particle extinction and linked to the average size of the particles in the plume), of the single scattering albedo (linked to the absorption properties of the aerosol layer) and of the asymmetry parameter (linked to the angular distribution of the aerosol layer) are selected for each case described in Sect. 4.5; please refer to this section for the details of these different hypotheses. Different runs are realized, for all experiment, for different sola zenith angles (SZA) to sample the full day. The daily-average shortwave TOA RF for the volcanically-perturbed aerosol layer is calculated as the SZA-averaged upward diffuse irradiance for the baseline simulation minus the volcanically-perturbed run, integrated over the whole shortwave spectral range. The shortwave surface radiative forcing is calculated as the SZA-average downward global (direct plus diffuse) irradiance for the volcanically-perturbed run minus the baseline, integrated over the whole spectral range.

2.3 Satellite Observations of volcanic plumes

2.3.1 SO2, SA and dust observations with IASI

The Infrared Atmospheric Sounder Interferometer (IASI) is a Fourier transform spectrometer covering the large infrared spectral range between 645 and 2760 cm^{-1}, with a relatively high spectral resolution (0.5 cm^{-1}) and a relatively small radiometric noise (noise equivalent spectral radiance of about 20 $mW/(cm^{-1}m^2sr)$ around 1000 cm^{-1}). The IASI instrument observes the Earth's

atmosphere and surface with a downward-looking geometry, with circular footprints of down to 12 km radius at the nadir spaced by 25 km, and with a swath of 2200 km (Clerbaux et al., 2009). The instrument series are on board MetOp-A -B and -C spacecrafts since 2006, 2012 and 2018, respectively. Each instrument of the series provides a near-global coverage every 12 h. For this work, we have used IASI observations of SO2, SA and dust.

The IASI daily SO2 dataset includes SO2 columns and volcanic plume altitude. The SO2 partial columns at 6 altitude intervals between 5 and 25 km are retrieved from IASI observations by exploiting the correlation between brightness temperature differences and SO2 total columns with assumptions on the SO2 plume altitudes (Clarisse et al., 2012). From these partial columns profiles, the total column is obtained by vertical integration. In addition, the altitude of the SO2 plume is estimated by using a sensitive trace gas detection method for high spectral infrared measurements (Clarisse et al., 2014).

The detection of SA and its aerosol-type-specific optical depth is provided by the AEROIASI-H2SO4 retrieval algorithm (Guermazi et al., 2021). The AEROIASI-H2SO4 algorithm is based on a self-adapting Tikhonov-Phillips regularization method, built around the radiative transfer model Karlsruhe Optimized and Precise Radiative transfer Algorithm (KOPRA) (Stiller et al., 2000). This method iteratively fits each IASI spectrum at 20 spectral micro-windows by adjusting the vertical profile of SA number concentration, jointly with water vapour profiles and surface temperature. The SA are assumed as spherical droplets of an aqueous solution of sulphuric acid (H2SO4), and the corresponding refractive indices are taken from Biermann et al. (2000). The information on the total SA-specific optical depth is mainly provided by the selective absorption of the undissociated H2SO4 in the SA solution droplets. The interference of the co-existent SO2 is avoided by using an operational spectral micro-window around 900 cm^{-1}, a spectral region characterised by H2SO4 absorption bands but outside the main SO2-sensitive region around 1100-1200 cm^{-1}.

For the characterization of the three-dimensional distribution of desert dust plumes during the event analyzed in the paper, we use the AEROIASI-Dust approach (Cuesta et al., 2015, 2020). The AEROIASI-Dust algorithm derives vertical profiles of desert dust, in terms of extinction coefficient at 10 μm, from individual thermal infrared spectra measured by IASI satellite sensor in cloud-free conditions, both over land and ocean. This method iteratively fits each IASI spectrum at 12 spectral micro-windows by adjusting the vertical profile of dust aerosol abundance jointly with surface temperature. The information on the vertical distribution of dust is mainly provided by their broadband radiative effect, which includes aerosol thermal emission depending at each altitude on the vertical profile of temperature. As for AEROIASI-H2SO4, the AEROIASI-Dust algorithm uses the radiative transfer model Karlsruhe Optimized and Precise Radiative transfer Algorithm (KOPRA) (Stiller et al., 2000). The current paper uses AEROIASI retrievals from version described by Cuesta et al., (2020) but using a complex refractive index derived by Di Biagio et al. (2017) with a dust sample from a desert in Mali (which shows a smaller difference between IASI and simulated spectra than that used by Cuesta et al. (2020)).

2.3.2 SO2 and AI observations with Sentinel-5p TROPOMI

The TROPOspheric Monitoring Instrument (TROPOMI), onboard the Copernicus Sentinel 5 Precursor (S5p) spacecraft, is a joint project of the Netherlands Space Office and the European Space Agency (Veefkind et al., 2012). The TROPOMI is a satellite-based spectrometer operating in the ultraviolet/visible/near infrared spectral region and at a nadir-viewing geometry. It provides observation of key atmospheric constituents at the unprecedented high spatial resolution of down

to 7×3.5 km^2. In the present work, we use the offline Level 2 datasets of Aerosol Absorbing Index and the total SO2 column.

The UltraViolet Aerosol Absorbing Index (UVAI) is a compact parameter used to visualize the presence of absorbing aerosols in the sampled airmasses. It is based on the spectral ratio of the measured top of the atmosphere reflectance and a pre-calculated theoretical reflectance for a Rayleigh scattering-only atmosphere, at a given pair of UV wavelength. Positive residuals of the observed and modelled reflectances are linked to the presence of UV-absorbing aerosols, like dust and smoke. Negative residuals may indicate the presence of non-absorbing aerosols, while values close to zero are found in the presence of clouds or no aerosols. As the UVAI is dependent on different aerosol layer optical and morphological properties, and on the underlying surface reflectance, in this paper we use this parameter only as a general indication of the presence of dust.

The total column SO2 is retrieved using a DOAS (Differential Optical Absorption Spectroscopy) method. The SO2 slant column density (SCD), i.e. the SO2 concentration along the mean light path through the atmosphere, is derived by fitting cross-sections in a spectral range characterised by the absorption of SO2 (in this case, at different spectral fitting micro-window between 310 and 390 nm, depending on the SO2 burden). After different calibrations and corrections of the derived SO2 SCD, this latter is converted to vertical columns using the air mass factor from radiative transfer calculations. For more details about the TROPOMI total column SO2 product, please refer to Theys et al. (2017).

2.3.3 SO2 observations with OMPS-NM

The Ozone Mapping and Profiler Suite Nadir Mapper (OMPS-NM) flies on the Suomi National Polar-orbiting Partnership (Suomi-NPP) satellite since 2012 and measures the Earth backscattered UV/visible radiation at a nadir-viewing geometry (Ditman et al., 2002). In this work, the Level 2 height-resolved SO2 product is used. For this product, a direct vertical column fitting algorithm is used to retrieve the SO2 column amounts in the lower (centered at 2.5 km), middle (centered at 7.5 km) and upper (centered at 11 km) troposphere, as well as the lower stratosphere (centered at 16 km).

2.3.3 Aerosol classification with CALIOP

The Cloud-Aerosol LIdar with Orthogonal Polarization (CALIOP) is a LiDAR system onboard the Cloud-Aerosol Lidar and Infrared Pathfinder Satellite Observation (CALIPSO) spacecraft ; it flies at about 700 km altitude in a sun-synchronous orbit and is part of the so-called A-Train (Winker et al., 2010). The CALIOP space LiDAR is in orbit since April 2006 and is still in operation. It provides vertical profiles of aerosols and clouds at about 01:30 and 13:30 local time. In this work, we use aerosol detections of the Vertical Feature Mask level 2 product version 4.2, at varying horizontal resolution, as well as the related aerosol types classification information.

2.4 Ground-based observations

2.4.1 MPLNET LiDAR observations at Sede Boker site

The National Aeronautics and Space Administration (NASA) Micropulse Lidar Network (MPLNET; Welton et al., 2001) project was established in 1999 in support of the NASA Earth Observing System (EOS; Wielicki et al., 1995). During the last two decades, MPLNET observations have significantly contributed to fundamental studies and applications on climate

change and air quality studies and in support for NASA satellite and sub-orbital missions (Lolli et al., 2018, Bilal et al., 2019, Lolli et al., 2020, Lewis et al., 2020, Campbell et al., 2021). This federated global network is constituted by homogeneous commercially available Micropulse LiDARs (MPL) instruments manufactured by Droplet Measurement Technology. The MPLNET instruments are single-wavelength LiDAR systems that use a diode-pumped Nd:Yag laser at 532 nm, with a 1-minute temporal resolution and 75-meter vertical resolution. The MPLNET network is active during the whole day and night and operates in all weather conditions, in the limit of laser signal extinction. The MPLNET network is deployed at global scale and cover all latitudes bands. For this study, the observations from Sede Boker (30.8° N, 34.8° E, 480 m a.s.l.) permanent MPLNET site are specifically used. To retrieve the vertically-resolved optical aerosol and cloud properties from a single wavelength LiDAR, strong assumptions, that limit retrieval accuracy, are needed. To reduce this uncertainty, MPLNET LiDAR network deploys the instruments, if possible, together with an Aerosol Robotic Network (AERONET; Holben et al., 1998) sun-photometer to constrain the LiDAR equation and reduce the retrieval errors (Welton et al, 2000). More details on the full MPLNET standard data product suite, including aerosols, have been provided by Welton et al. (2018). The standard, automated, MPLNET products are not designed to accurately capture elevated volcanic plumes due to their transient nature, high altitude, and unique microphysical properties relative to the local aerosols that limit the usefulness of the constrained aerosol retrieval approach. Instead, MPLNET provides a custom retrieval method that bypasses the automated aerosol height algorithm, and requires manual specification of the plume altitude (for this study based on inspection of the lidar signal and volume depolarization ratio profiles). Upon specification of the plume base and top, the optical depth of the plume is determined using the attenuation of the lidar signal and a molecular scattering (Lewis et al, 2016). The retrieval of plume properties is calculated using the same MPLNET constrained retrieval algorithm using the plume optical depth. This process often results in few retrievals during the plume's advection over the lidar site as calculation of the plume optical depth is difficult with noisy signals. Instead, the Lidar Ratios from these few retrievals are averaged, and the result is used to determine the plume properties by fixing the Lidar Ratio using the classic Fernald lidar algorithm (Fernald 1984). The retrieved lidar ratios were in good agreement with several LiDAR studies on volcanic emissions (e.g., Prata et al., 2017) and a fixed value of 50 sr was used. Data is freely available on MPLNET website (https://mplnet.gsfc.nasa.gov/).

2.4.2 The ACTRIS-Fr OHP LiDAR Observatory

The Observatoire de Haute-Provence (OHP) located in southern France (43.9° N, 5.7° E, 670 m a.s.l.) is one of the NDACC (Network for the Detection of Atmospheric Composition Change) alpine stations, equipped with a variety of LiDAR instruments for monitoring of the lower and middle atmosphere.

The longest continuous LiDAR data record at OHP is provided by a Rayleigh-Mie-Raman LiDAR for temperature and aerosol measurements (hereafter referred to as LTA) operating at the wavelength of 532 nm. The LTA instrument (Keckhut et al., 1993) has provided routine measurements for over 3 decades with a mean measurement rate of 10-12 nighttime acquisition nights per month and a typical duration of acquisition of 3-5 hours. To retrieve the vertical profiles of aerosol backscatter and extinction, the raw lidar returns from three LTA elastic channels, covering respectively troposphere, lower stratosphere and upper stratosphere, are merged and a Fernald-Klett inversion method is applied (Fernald, 1984), assuming a constant LiDAR ratio of 50 sr. The retrieved backscatter and extinction coefficients are reported with a time resolution of 1

minute and a vertical resolution of 15 m. The scattering ratio is then computed as a ratio of total (molecular plus aerosol) to molecular backscattering, where the latter is derived from ECMWF meteorological data. A more detailed description of the instrument, aerosol retrieval and error budget is provided by Khaykin et al. (2017) and references therein.

The ultraviolet tropospheric differential absorption LiDAR (LiO3tr) also operated at OHP at the same time as the LTA LiDAR. It records backscatter signal at 316 nm for ozone monitoring (Ancellet et al. 1997, Gaudel et al. 2015). The 316 nm signal is very weakly absorbed by ozone in the troposphere and can be used for aerosol backscatter monitoring between 3 and 13 km altitude. As for the LTA instrument, the Fernald-Klett inversion method (Fernald, 1984) is applied assuming a constant LiDAR ratio of 50 sr at 316 nm and a 1.01 scattering ratio close to a molecular return at 11 km. Since no overlap correction is applied in order to match the LTA retrieval at 3 km, a scattering ratio uncertainty of the order of 10% is expected below 4 km.

The OHP observatory is also equipped with an automatic LiDAR (CIMEL model CE376) sounding in the troposphere from ~200 m to ~12 km of altitude at the wavelength of 532 nm, named GAIA and operational since 2019. The GAIA system is also equipped with a depolarization channel at the same wavelength to gather more information on the nature and optical properties of aerosols, mostly in the boundary layer and in the free troposphere. It provides data at a frequency of 1 mn and the datasets are then averaged on 10 min slices. Its spatial resolution is 15 m. The scattering ratio is computed as for the LTA LiDAR, but interpolating radiosoundings collected at OHP launched every week in the late morning. The data are corrected for instrumental deadtime, overlap in the first hundreds of meters of altitude (using an algorithm called CHECK delivered by the PHOTONS-AERONET network), sky background and squared altitude to take into account the quadratic decrease of the signal in function of altitude. A Haar wavelet method (Brooks 2003, Cohn and Angevine 2000) can then be used to retrieve the boundary layer height. The GAIA data are inverted using the Klett method (Klett 1981).

2.4.3 The ACTRIS Napoli LiDAR observatory

The Napoli LiDAR observatory (Naples, Italy, 4.18° E, 40.84° N, 118 m a.s.l.) is part of the ACTRIS (Aerosol, Clouds and Trace Gases Research Infrastructure) research infrastructure, a pan-European distributed research infrastructure for short-lived atmospheric constituents producing high-quality data in the area of atmospheric science (Wandinger et al., 2020). The Napoli observatory includes passive and active remote sensing systems and near-surface sampling systems, for atmospheric studies. Thanks to its quite central location in the Mediterranean basin, it represents a strategic location to study optical and microphysical properties of the aerosols coming from local sources and long-range transport.

The station is equipped with a multiwavelength elastic/Raman LiDAR device able to detect elastic signals at 355 nm, 532 nm and 1064 nm, Raman N2 echoes at 386 nm and 607 nm and aerosol depolarization at 532 nm. Details on this LiDAR system are reported by Boselli et al. (2021). Vertical profiles of the aerosol extinction coefficient and linear depolarization ratio are shown and discussed in this paper. The aerosol extinction coefficient profiles were retrieved using the procedure introduced by Ansmann et al (1990). The calibrated particles linear depolarization profiles were obtained from the backscattered light polarized along both perpendicular and parallel

directions respect to the laser beam polarization and following the inversion procedure reported by Biele et al. (2000) and Freudenthaler et al., (2006).

2.4.3 The AERONET observations

Total column measurements of the aerosol optical depth (AOD), Ångström exponent and single scattering albedo at several wavelengths, among others aerosol parameters, are carried out globally with Cimel sun photometers, as part of the AErosol RObotic NETwork (AERONET; see the AERONET website at http://aeronet.gsfc.nasa.gov and the description by Holben et al., 1998, for further details). In this manuscript we use the AERONET observations for these three aerosol parameters at the selected station of Sede Boker, OHP and Napoli, which are part of the AERONET network.

3 The Mount Etna activity in February and March 2021

Between February and April 2021, Mount Etna experienced an intense eruptive activity from the South East Crater (SEC) consisting of astonishing short-lasting lava fountain eruptions coupled with lava effusion and episodic pyroclastic density currents. The activity took place while all the summit craters, Bocca Nuova, Voragine, North-East crater, where displaying a mild strombolian activity and lava effusion at Voragine and Bocca Nuova craters continuously since September 2019. Differently than the other three summit craters, over the same period SEC was episodically erupting but featured a slow and gradual energy increase of its eruptive activity. Eruption, eventually intensified between December 2020 and January 2021 to abruptly escalate on the afternoon of 16 February 2021, starting to produce a sequence of lava fountaining which ended on 1st April 2021. Over these two months, 17 paroxysmal episodes were produced with a recurrent characterisation, consisting of the resumption of strombolian activity growing in intensity, lava flow effusion, and transition from discrete explosions to the continuous gas and lava jetting typical of lava fountaining. Overall, each lava fountain lasts few hours while producing the sudden spreading in the atmosphere of a volcanic ash and SO2 plume that rose for a mean altitude of 10 km asl. Each eruptive episode was accompanied by the dispersal of ash plumes and fall-out deposits in the surrounding towns of the volcano up to Catania, which often pose severe hazards to aviation and repeated temporary closures of the Catania international airport. Lava flows propagated mostly in the eastern flank of the volcano in the Valle del Bove and remained confined at a mean altitude of 2,700 m asl. In the present study we focus on the specific phase, during this broad activity, occurring between the 21 and 26/02/2021. Three main short-lived paroxysmal events, discussed in Sec. 4.1, occurred during this time period.

4 Results

4.1 Three paroxysms in four days: the SO2 emissions

The method described in Sect. 2.1 was applied to the SEVIRI observations of 21-26/02/2021 to estimate the SO2 emission rate and altitude of plume injection for the three individual paroxysms in this timeframe. In Fig. 1, the temporal profile of the emission rate and altitude, for the Events #1, 2 and 3 (whose dispersion is subsequently associated to the three plumes referred to as plumes P1, P2 and P3 in Sect. 4.2) are shown. The SO2 emissions associated to the Event #1 started at about 23:00 of 20/02 and sharply increased during the first hours of the day 21/02. The emission rate for this event peaked at values of about 2000-2500 kg s^{-1} at 01:00 to 02:00 of 21/02. During

this event, the injection altitude is also sharply increasing from the crater altitude to about 12 km, peaking between 01:00 and 02:00 of 21/02. The SO2 emissions for the Event #1 sharply decreased afterwards and the paroxysm was over by about 04:00 of 21/02. The Event #2 started at about the same time but one day later than Event #1. The Event #2 had a sensibly shorter duration than Event #1 - it started at about 23:00 of 21/02 and was over by 01:00 of 22/02 - but its peak emission rate is nearly twice as large than for the Event #1, peaking at about 5000 kg s^{-1} on 22/02 00:00. The injection altitude for the Event #2 peaks at 12 km, in a similar fashion as the Event #1. At about 19:00 of 24/02, the Event #3 kicked off. The temporal profile and duration of the SO2 emission rate and injection altitude for the Event #3 is similar to those of the Event #1, with a slightly smaller peak value of the emission rate (1500-2000 between 20:00 and 22:00 of 24/02).

The total emitted SO2 mass for the three events has been estimated at values of 19.3, 20.9 and 14.6 kt for the Event #1, 2 and 3, respectively. The Event #2 injected the largest amount of SO2, despite the shortest duration for the ensemble of the three events, due to the significantly larger peak emission rate. The total SO2 mass emitted from the three added events is 55 kt. Typical values of the emission rates for moderate-to-strong eruption of Mount Etna are generally less than 2000 kg s^{-1} (Sellitto et al., 2016, Corradini et al., 2020). This specific activity is then characterised by relatively brief but very intense paroxysmal events, if compared to more general behaviour of Mount Etna. In addition, the altitude of the plume injection is particularly high. Documented extremely high-altitude eruptions of Mount Etna rarely exceed 10-11 km altitude (e.g. Sellitto et al., 2016, Corradini et al., 2020). Thus, this series of three paroxysms qualify as an extreme event in terms of the injection altitude. The total SO2 mass emitted during these few days of activity is about 50% of the record-breaking sequence of eruptions of 24-31/02/2015, which was estimated, with a similar method as the present paper, at about 100.0 kt overall (Corradini et al., 2020). Thus, in terms of the SO2 emission rates and injection altitude, as well as for its total SO2 emitted mass, the sequence of three events during 21-26/02/2021 has to be categorised as one in the higher spectrum of eruption strengths of Mount Etna.

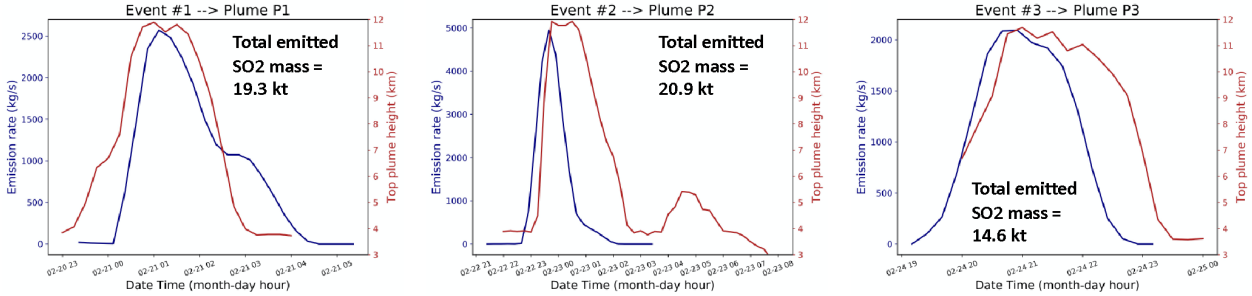

Figure 1: Temporal profile of the emission rates (blue lines) and injection altitude (red lines) for the three paroxysmal events (Event #1-3 in the figure) of Mount Etna in the period 21-26/02/2021. The total emitted SO2 mass, for each of the three events, is also reported in the individual panels.

4.2 An uncommon transport toward the north: the SO2 plume dispersion

The plumes emanating from the three individual paroxysmal events described in the previous section are then characterised in terms of their subsequent dispersion.

Figures 2-4 show the SO2 column amount and plume altitude obtained from IASI observations, and the SO2 column amount obtained from FLEXPART simulations, for 21-22 (Fig. 2), 23-24 (Fig. 3) and 25-26/02 (Fig. 4). The FLEXPART SO2 simulations are obtained using the measured SO2 emissions described in Sect. 4.1. As extensively discussed by Sellitto et al. (2016), the synergy of good quality regional observations from satellite and realistic simulations is crucial to get more comprehensive insight into confined plumes dispersion, thanks to the information

complementarity of these two information layers. In fact, the vertical sensitivity of satellite observations of SO2 is limited, thus satellite observations can only provide a partial information on the height distribution of SO2; on the other hand, uncertainties in the input parameters and the physico-chemical in-plume processes can impact on the realism of dispersion simulations. In addition, the temporal sampling of satellite observations, one or two overpasses per day for low-Earth orbit spacectaft, is usually not sufficient to smoothly characterise the temporal evolution of the plume's dispersion. On the contrary, dispersion simulations can be realised at sub-hour temporal resolution, thus filling the temporal gap between satellite overpasses. An animation of the FLEXPART simulations for this case study, with the full temporal resolution of 30 minutes, can be found as Supplement. As it is possible to notice from Figs. 2-4, the description of the plume dispersion with observations and simulations is very consistent, thus cementing our confidence in our further interpretation of the plumes dynamics.

On 21/02, the plume P1, linked to the paroxysmal Event #1, disperses towards the central Tyrrhenian Sea, reaching Corsica to the western coast of Tuscany, for the night overpass of IASI (about 21:30 LT). During this phase, the plume stayed between 10-12 km altitude, with lower-altitude sections at the southern end of the plume. Values slightly higher than 15 DU are found for plume P1 during this phase, both from observations and modelling. The plume P1 then dispersed towards more north-eastern direction on the 22/02, to northern Italy and then Austria and further north-east, while progressively slightly descending at lower altitudes (down to 8-10 km). Clusters of relatively large values of the SO2 column, around 15 DU, are found on 22/02. Plume P1 orientates around an anticyclonic circulation due to the presence of a stable Omega block in Central Europe (Hoshyaripour, 2021), dispersing towards the south-eastern direction on 23/02 and then disperses further east, reaching Turkey and the Middle East on 24/02. The SO2 column concentration for P1 remained relatively large, with values larger then 10 DU, while the plume kept descending, down to 7-10 km on 24/02. On 23/02, plume P2 (linked to the paroxysmal Event #2) kicked off with a similar initial dispersion as for P1, towards the central Tyrrhenian Sea, before starting to spread on 23/02 afternoon, from southern France to the Adriatic Sea. By 24/02, the plume P2 has formed an elongated and almost filamentary shape of quite large horizontal extent, from northern Spain, to the west, to southern Greece, to the east. Plume P2 was also much more irregular, in terms of both SO2 column amount and plume altitude than plume P1. Values as high as 15 DU are found at the western and eastern ends of the plume, with mean altitudes at about 9 to 12 km. Smaller column values, around 5-6 DU, and a mean altitude of about 10 km are found in the central area of the plume, in sub-alpine northern Italy. Plume P2 then compressed (i.e. the western and eastern ends of the plume got closer) on 25/02 and formed a curly plume then starting to disperse towards the north-east on 26/02. During this phase, the eastern end of plume P2 swept through southern Italy, still keeping at 8-9 km altitude. Plume P3 (linked to the paroxysmal Event #3) appears on 25/02 morning, again orientating towards the central Tyrrhenian Sea, while rapidly dispersing towards the east together with plume P2. Plume P3 displayed slightly larger values of the SO2 column (larger than 15-18 DU) and lower altitude (7-10 km) than plumes P1 and P2. This overall description of the dispersion of the plumes P1-3 in the upper-troposphere (UT) is confirmed

by the independent observations of the upper-tropospheric SO2 column from OMPS-NM (Supplementary Fig. 1).

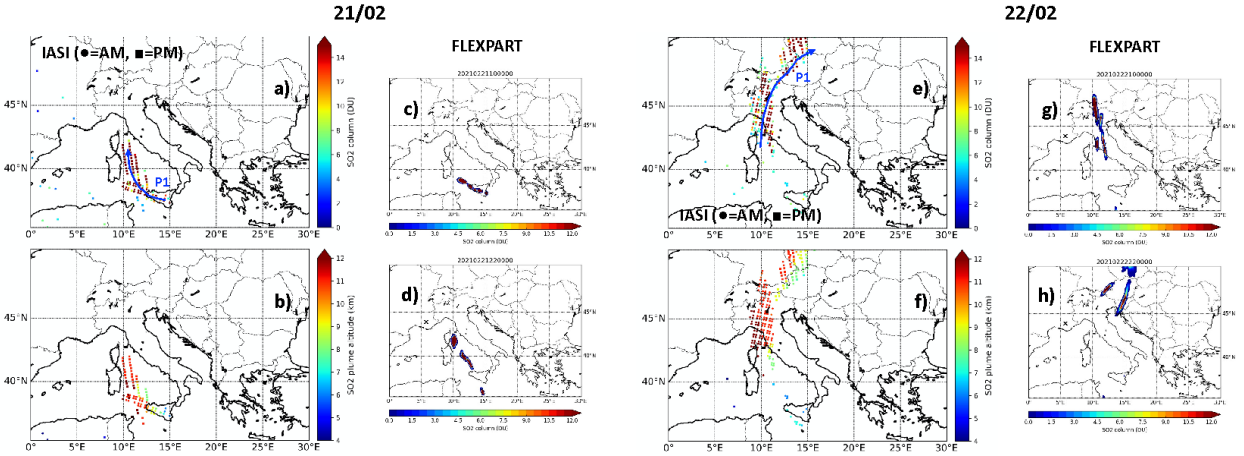

Figure 2:IASI SO2 column (a,e) and mean altitude of the plume (b,f) for the morning (approximate overpass at ~9:30 LT, circles) and afternoon (approximate overpass at ~21:30 LT, squares) MetOp-A spacecraft overpass; corresponding FLEXPART SO2 column simulations (at 10:00 LT, c,g, and at 22:00 LT, d,h), for 21 and 22/02/2021. Plume P1 is individuated, and its approximate direction of dispersion is indicated as a blue arrow in panels a and e.

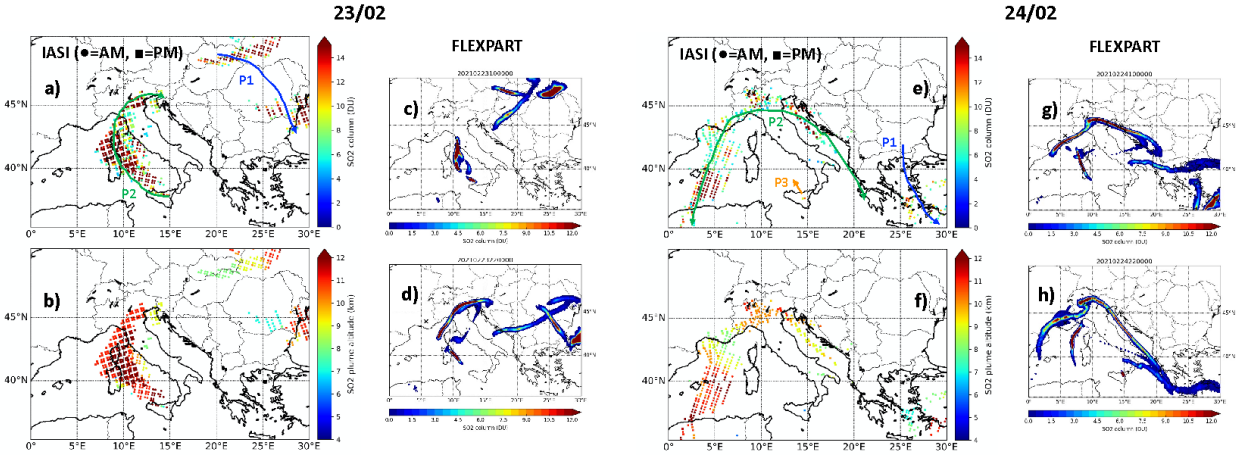

Figure 3: same as Figure 2 but for 23 and 24/02/2021. Plumes P1, P2 and P3 are individuated, and their approximate directions of dispersion are indicated as blue, green and orange arrows, respectively, in panels a and e.

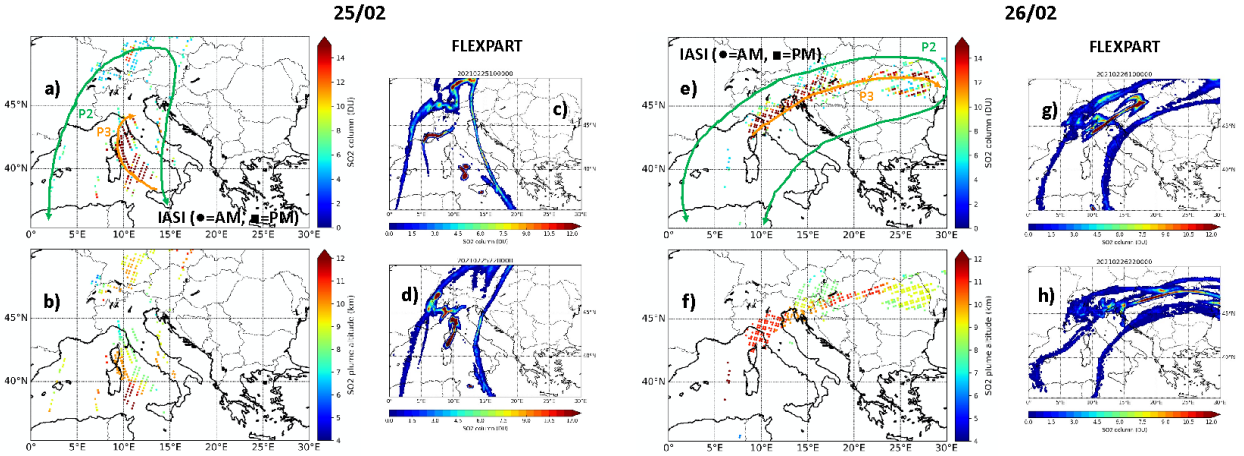

Figure 4: same as Figure 2 but for 25 and 26/02/2021. Plumes P2 and P3 are individuated, and their approximate directions of dispersion are indicated as green and orange arrows, respectively, in panels a and e.

More in general, the dispersion of plumes P1-3 was consistently directed towards the northern quadrant from the perspective of the Mount Etna volcanic source. Using a more-than-one-decade long dispersion simulations dataset, Sellitto et al. (2017) have estimated the prevalent direction of dispersion of the plumes generated from Mount Etna emissions. They have found that for more than 80% of the time Mount Etna's plumes disperse towards the eastern quadrant. The dispersion towards the northern and north-western quadrant, as is the case for the initial dispersion for these events, is a rare occurrence, accounting only for less than 5% of the cases. On the other hand, the northern and north-western sectors are the only downwind areas that assure the presence of continental long-term active observatories that can allow the downwind observation and characterisation of Mount Etna's plumes. Thus, this series of paroxysms is a rare occasion to study more in details the dispersed plume of Mount Etna's volcanic emissions.

4.3 Not only volcanic aerosols: the dust events of February 2021

During the same period of the series of volcanic events discussed in this manuscript, a major Saharan dust outbreak to central Europe occurred (Hoshyariapour 2021). Starting from 21/02, a trailing cold front produced a sustained dust uptake in northern Morocco and Algeria; the dust was then transported towards western Europe by southerly flow, was lifted by warm conveyor belt, and entered the mentioned Omega block located in central Europe, thus orienting in an anticyclonic circulation similar to volcanic plume P1. More specific analysis of this dust event is beyond the scopes of the present paper. Nevertheless, here we characterise the bulk dust distribution during this event, so to help the interpretation of the volcanic plumes at downwind observatories of Sect. 4.4.

Figures 5a-e display the UVAI observations from TROPOMI during this period. They show the dust emitted from north-western Sahara towards the Western Mediterranean and North-Eastern Spain on 21/02, thus reaching Central and Northern France on 22/02 and then circulating around the Omega block high pressure during the following days, with weaker and weaker UVAI signature, possibly do to dust removal and dispersion. The vertical distribution of Saharan dust for this event is further investigated using the height-resolved information of the AEROIASI-Dust algorithm. In Fig. 5f, the dust-specific aerosol extinction profiles at 10 μm, from AEROIASI-Dust,

is shown for the 24/02. The dust looks confined, in the region of interest of our study, between 3 and 6 km altitude.

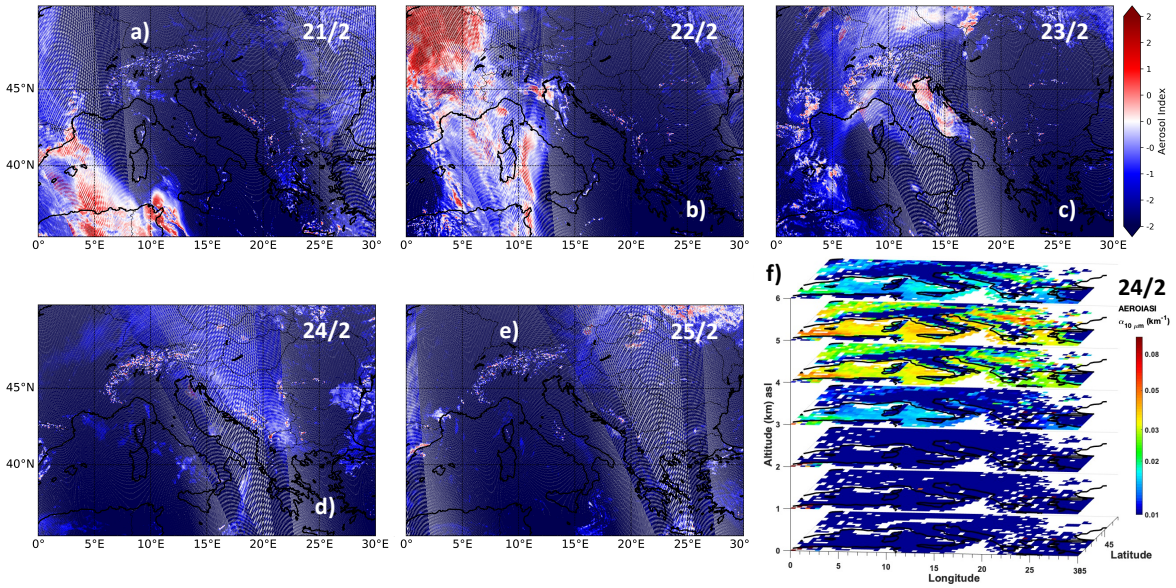

Figure 5: UVAI retrievals with S5p TROPOMI for the period 21-25/02 (a,e). Dust-specific aerosol extinction at 10 μm from AEROIASI-Dust observations for 24/02, from surface to 6 km altitudes (f).

Figure 6a,b show the CALIOP feature layer classification for CALIOP day and night overpasses in the area of interest (see ground tracks of CALIOP in Fig. 6c), on 24/02. Both day and night overpasses confirm the presence of dust from near-surface to 5-7 km altitude. The lifting of the dust layer in the south-north direction, from North Africa to Central Europe, is clearly visible. Figure 6b also shows evidence of the volcanic plume from Mount Etna plume P2. As discussed more in details in Sect. 4.4, the plume P2 arrives in Southern France and Spain coastal areas on 24/02 afternoon, which is consistent with the two CALIOP overpasses of Fig. 6a,b. An early observation of the plume P2 on 23/02, in the central Tyrrhenian Sea, together with the underlying dust layer, is shown in the Supplementary Fig. 2. The volcanic aerosol layer is reasonably co-located with the volcanic SO2 plume, observed with TROPOMI, for both overpasses (23/02, Supplementary Fig. 2b, and 24/02, Fig. 6c). The volcanic plume P2 observed by CALIOP, is located at exceptionally high altitudes for Mount Etna's activity, at 12-13 km on the 23/02 and then slightly descending to 11-12 km on 24/02. The vertical plume location is very consistent with IASI observations and FLEXPART simulation of the SO2 plume discussed in Sect. 4.2. The volcanic and the dust plumes remain completely vertically-separated in this area.

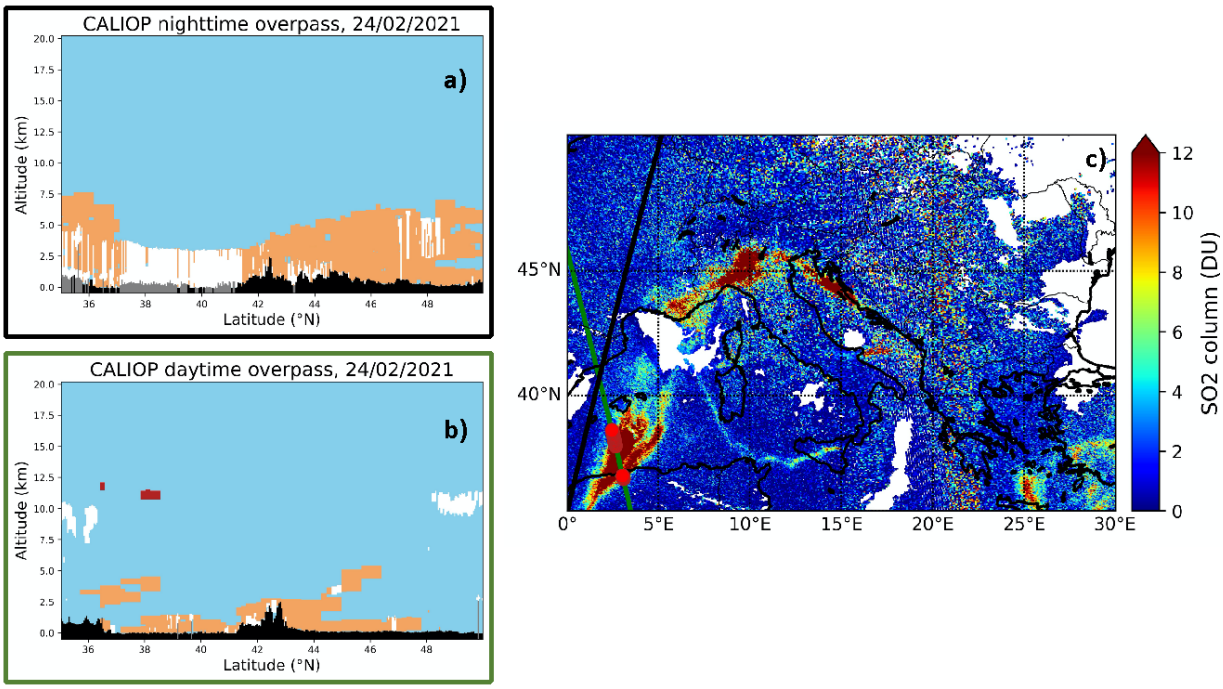

Figure 6: (a,b) Feature layer classification (sky blue: clear sky, black: Earth's surface, white: clouds, brown: tropospheric aerosol – here classified as dust, red: stratospheric aerosol feature – here classified as volcanic, grey: no signal) for CALIOP nightime, at ~2:00 am (a) and daytime, at ~1:30 pm (b), overpasses for 24/02/2021. (c) Sentinel-5p TROPOMI SO2 column observations for 24/02/2021. The black and green lines in panel c are the ground tracks of CALIOP observations of panel a and b, respectively. The position of the stratospheric aerosol (volcanic) feature, identified in panel b, is also indicated in panel c as red circles.

4.4 The volcanic plumes themselves: observations at downwind observatories

The uncommon transport of Mount Etna's plumes towards the north, for these three events, is a rare occasion to monitor and characterise the volcanic aerosols in Mount Etna's plumes at well-equipped observatories, including vertical information with LiDAR systems. As mentioned above, in the large majority of cases, Mount Etna's plumes disperse towards the east, in a mainly marine region where very few ground observation stations are present. On the contrary, there is significant density of ground stations northwards, i.e. in continental Europe.

Plumes P1 and P2 have been observed downwind at different stations. Here in the following, we analyse the plume's observations at three stations: Sede Boker, Israel, OHP, France, and Napoli, Italy.

Figure 7a shows the volcanic plume vertical distribution over Sede Boker station, in terms of the SO2 volcanic tracer, from FLEXPART simulations. Figure 7b shows the series of LiDAR aerosol observations at Sede Boker, for the same period. The plume P1, after a relatively long dispersion phase over central-easter Europe, driven by anticyclonic flow of the Omega block discussed in Sect. 4.2 (see Fig. 2 and 3, as well as the animation in the Supplementary material), overpasses the Sede Boker station starting from 25/02 early in the morning and, with discontinuous broken dispersed plumes sections, until 26/02 in the early afternoon, as visible from Fig. 7c. More dense clusters of the plume P1 overpass the station during the period spanning from 25/02 night to 26/02 early morning. During this plume's overpass, P1 has aged 4-5 days since their volcanic emissions. The LiDAR observations show an aerosol layer linked to the plume P1 in the same period indicated by the FLEXPART simulations. Even if a part of the plume observation is missed by the LiDAR,

during the night between 24 and 25/02 (due to low LiDAR signal quality), a consistent vertical behaviour is shown by simulations and observations. Both information layers show an initially higher plume, located at 9-10 km, then descending to 5-6 km altitude. The plume looks filamentary, with a geometrical vertical thickness of less than 500 meters (Figs. 7a and b) and a horizontally-confined shape (Fig. 7c). The mean aerosol depolarization for the plume is 32.3±1.4% (Tab. 1). This value is very elevated for volcanic aerosols and might indicate the presence of a large fraction of fine ash, for plume P1. The three-dimensional morphology of this aerosol layer, as detected by LiDAR, as well as the consistency of observations with volcanic tracer dispersion simulations, suggest that a significant presence of dust can be excluded at these altitudes.

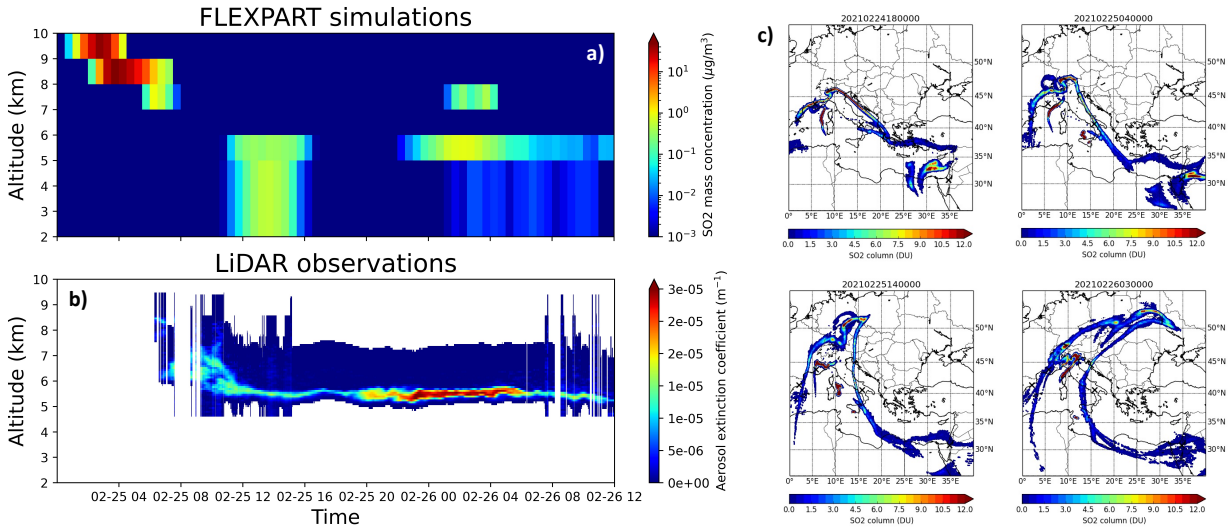

Figure 7: FLEXPART SO2 mass concentration profiles, from 25/02/2021 00:00 to 26/02/2021 12:00, over Sede Boker station (a). Volcanic-aerosol-specific LiDAR observations of the aerosol extinction coefficient, for the same period as in panel a, at Sede Boker station (b). Selected maps of the SO2 total column dispersion, between 24/02 and 26/02/2021, from FLEXPART simulations (c). The position of the Sede Boker station is shown as a black cross in panel c.

The western and eastern peripheries of the dispersed plume P2 (hereafter referred to as P2/W and P2/E, respectively) are almost synoptically observed at OHP (P2/W) and Napoli (PE/E) ground stations. Starting from 24/02, the plume P2 takes an elongated and then folded-shaped geometry, with the western periphery P2/W slowly moving south-westwards over Southern France and Eastern Spain, and the eastern periphery P2/E sweeping Southern Italy in a north-western direction (Fig. 3-4).

Basing on FLEXPART simulations, the P2/W section arrives at OHP station basically in two separate phases: during evening/night of 24/02 and during night/early morning between 25 and 26/02 (Fig. 8c). The FLEXPART simulations over OHP show a denser volcanic plume, in terms of the SO2 tracer, at altitudes of about 9-10 km altitude, with less dense volcanic plume at lower altitudes (2-4 km). This is generally consistent with the observations of the LTA LiDAR system at OHP (Figs. 8d-e). The LTA LiDAR was operational from about 18:30 to 22:30 on 24/04 and 25/02; it observes an aerosol layer at about 10-11 km altitude on both days and during the full period, with a maximum value of the aerosol extinction between 19:00 and 21:00 on 24/02, consistently with FLEXPART simulations. The very weak volcanic aerosol signature at 10-11 km for LTA LiDAR observations 25/02 is not present in FLEXPART simulations. A previous observations session was carried out during the late afternoon/evening of 23/02 (not shown here); a volcanic-related aerosol plume is not observed during this period, consistently with FLEXPART

time-series analyses of the plume P2/W dispersion. While the LTA LiDAR system was operational only during night-time, the co-located GAIA system observed the atmosphere over OHP during day-time as well (data not shown here), even if with a significantly lesser signal/noise ratio at those altitudes. While GAIA observes the same night-time volcanic aerosol signature as LTA (discussed above), no aerosol signature is present during the days of 24 and 25/02, so it is reasonable to exclude that volcanic aerosols were present in the atmosphere over OHP during the day. Besides the relatively high-altitude aerosol layer observations, the LTA LiDAR observed a lower-altitude aerosol plume at 3-5 km (see Fig. 8a). This aerosol signal can be easily associated with the dust event described in Sect. 4.3, even if a component of volcanic aerosol cannot be excluded based on the FLEXPART vertical profiles of Fig. 8c. For a limited time, the LTA and the LiO3t LiDARs operated simultaneously at OHP. Using a combination of the aerosol backscattering profiles retrieved by LTA (at 532 nm) and the LiO3t (at 316 nm) LiDARs at OHP, a colour ratio has been calculated in the free troposphere on 24/02 between about 19:00 and 20:30. The aerosol backscattering profile observations at both wavelengths show a vertically thin plume at about 10-11 km and a wider plume between 3 and 5 km. Besides this quite distinct vertical structure, the colour ratio shows very different values for the two layers, with 0.1-0.2 for the highest first layer and up to 1.0-1.2 for the lowest layer. In addition, depolarisation ratio observations with the GAIA system for the highest layer display very small, near-zero values. These evidences indicate the presence of distinctly smaller mean particle size, with a possible spherical shape, for the highest layer with respect to the lowest, thus corroborating the possibility that volcanic aerosols, with an SA prevalence, and dust, respectively, dominate the two layers. Spectroscopic evidence of the presence of SA at OHP is found using the AEROIASI-H2SO4 retrieval algorithm (Supplementary Fig. 3), this suggesting that the volcanic plume P2/W is composed of SA, even if the presence of an ash fraction cannot be excluded.

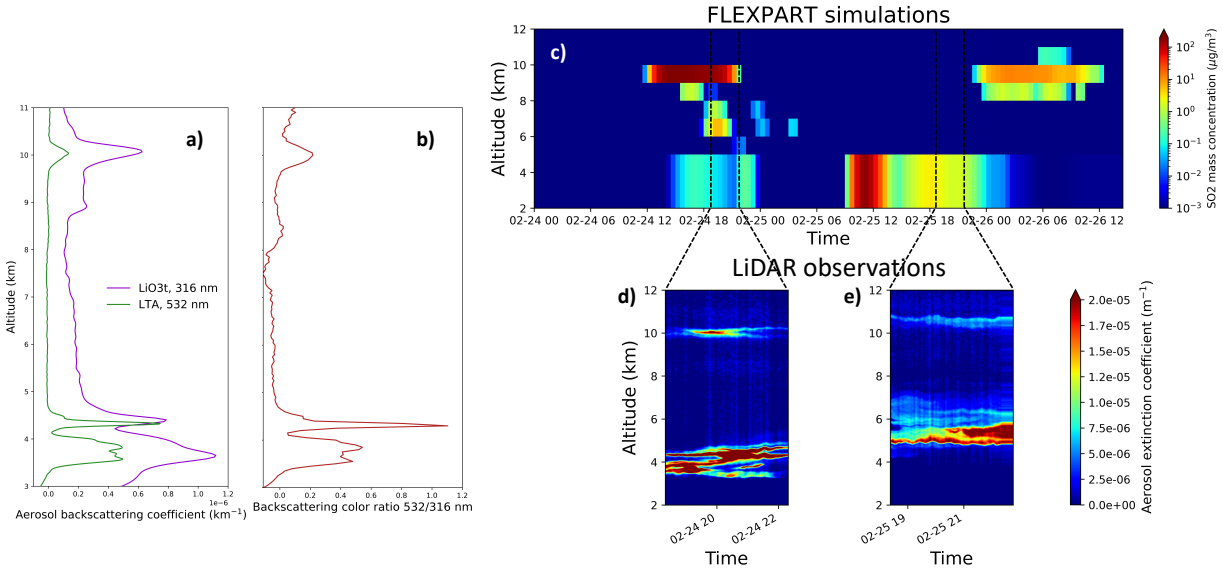

Figure 8: Mean aerosol backscattering coefficient profiles, between 19:00 and 20:30 of the day 24/02/2021, observed by LiO3t (violet line) and LTA (green line) LiDARs (a), and the backscattering colour ratio (b), at OHP station. FLEXPART SO2 mass concentration profiles, from 24/02/2021 00:00 to 26/02/2021 12:00, over OHP station (c) and available night-time LTA observations of the aerosol extinction coefficient in the same period (d: 24/02; e: 25/02). Time intervals of LTA observations are indicated by black dashed lines in panel c.

The P2/E plume section is observed at Napoli station. Based on the FLEXPART simulations, the P2/E volcanic plume overpasses Napoli during the period spanning from late morning to early

evening of 25/02, at an altitude of 7-10 km, with a maximum density between 15:00 to 18:00 (Fig. 9b). Consistently, the LiDAR system in Napoli observed a vertically-confined aerosol plume in the afternoon of 25/02, with a maximum around 17:30, at 7-8 km (Fig. 9a). A second aerosol plume, with a wider vertical structure, is observed between 2 and 3 km. The LiDAR system in Napoli operates at two wavelengths and has depolarisation information (depolarization ratio δ). Using the two wavelengths, the bulk Ångström exponent (AE) has been calculated. Both AE and δ show distinct values for the two layers: AE of 0.85 and 0.24, and δ of 10.1±5.8% and 26.6±1.7%, for the higher and lower layer, respectively. This indicates significantly smaller (AE observations) more spherical-shaped (δ) for the higher layer, thus corroborating the identification of the highest layer as volcanic and the lowest as dust. The AE and δ for the highest layer are nevertheless quite different from what expected for a pure SA-dominated layer, indicating the possibility of the presence of a fraction of larger and aspherical ash particles. It is also important to notice that: 1) the SO2 plume tracer of P2/E in Napoli (Fig. 9b) has peak values nearly two orders of magnitude larger than for P2/W at OHP (Fig. 8c), and 2) the aerosol extinction is almost ten times larger for P2/E (Fig. 9a) than P2/W (Fig. 8d). This clearly indicates the large variability of the morphology and properties of one volcanic plume, e.g. when looking at different plume's sections.

Based on the results shown in this section, two main evidences emerge: 1) precise (e.g. in terms of the input parameters) and detailed dispersion simulations, as well as complementary satellite observations at a wider regional scale, as support towards the interpretation of downwind observations, and 2) synoptic downwind observations at different locations, can be used to characterise in details confined plumes of known source and their variability in three-dimensional morphology, composition and properties. In the present case, for example, two separate and non-mixing vertical layers of volcanic aerosols and dust could be identified. For the volcanic aerosol layer, the variability of the vertical structure and composition at different sections of the plumes (see the case of plumes P2/W and P2/E), as well as the different properties of individual plumes for a given geophysical event (see the comparison of P1 and P2), could be characterised.

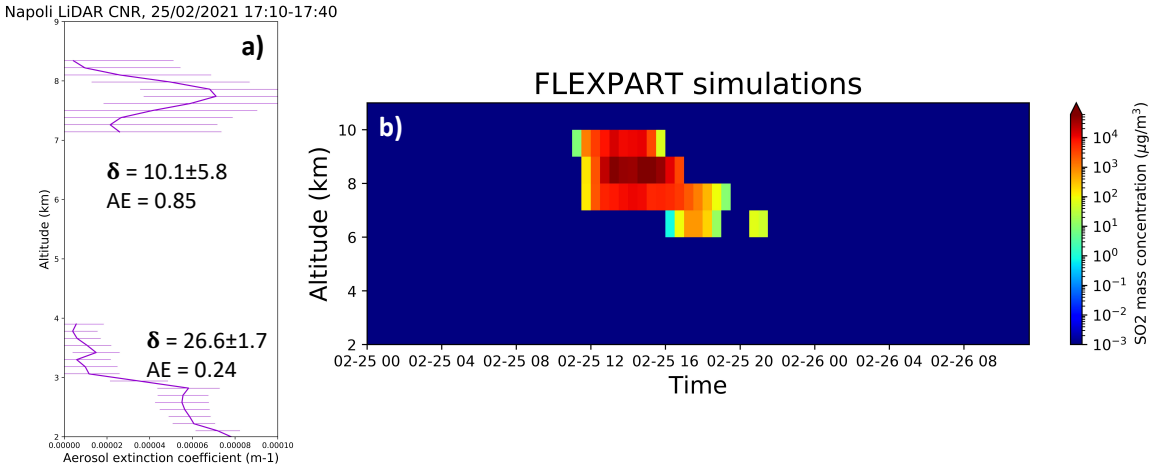

Figure 9: Mean aerosol extinction coefficient profiles at 355 nm, between 17:10 and 17:40 of the day 25/02/2021, observed by LiDAR (a) and FLEXPART SO2 mass concentration profiles, from 25/02/2021 00:00 to 26/02/2021 12:00, over Napoli station (b). The mean Ångström exponent (AE) and depolarisation ratio (δ), for the two identified vertically-separated aerosol layers are also reported in panel a.

678 4.5 Optical properties and the impact on the radiative balance

679 Using the observations from ground-based LiDAR and the complementary observations and
680 atmospheric modelling of the previous sections, the optical and radiative properties of plumes P1
681 and P2/E and W, at Sede Boker, OHP and Napoli stations, have been estimated.
682 The volcanic-specific aerosol optical depth (AOD_V), averaged during the core overpass periods
683 (see details in the caption of Tab. 1) at the three ground stations, estimated using LiDAR data, are
684 listed in Tab. 1. These values are also compared with the total column (i.e. volcanic plus dust and
685 other possible aerosols in the line of sight of the instrument) AOD_T, AE_T and SSA_T estimated with
686 co-located AERONET Cimel sun photometers. For plume P1, moderate AOD_T are found, with
687 relatively high AE_T, which points at a limited impact of dust in the overall column. The AOD_V is
688 relatively large, 0.0076 ± 0.0015. As mentioned, the large δ_V, aggregated with a relatively large
689 AOD_V, may point at a consistent presence of ash within the identified volcanic plume P1. This is
690 somewhat surprising for a plume that, at the time of downwind observation, has already aged about
691 4-5 days since emissions. It is worth noticing that this plume shows a consistent descent during
692 the dispersion (emitted at about 12 km and detected at Sede Boker at 5 to 10 km) which can be
693 linked to the larger sedimentation rate of the more massive ash particles than SA. As already
694 discussed in the previous section, plume P2 looks very inhomogeneous, when comparing the
695 western and easter ends P2/W and P2/E. This is mirrored by inhomogeneities in the measured
696 AOD_T. The P2/W plume has almost ten times smaller AOD_T with respect to P2/E (P2/W:
697 0.0036 ± 0.0014, P2/E: 0.031 ± 0.006). As discussed in Sect. 4.4, this large difference in the AOD_T
698 of P2/W and E can be attributed to the fact that these plumes may be largely dominated by SA, the
699 first, and may present a fraction of ash, the second. With AOD_T between 0.25 and 0.30, the total
700 column looks largely dominated by dust, with the volcanic component taking only a small part of
701 the column. Relatively small AE_T seems to confirm this hypothesis through the indication of the
702 dominance of very large (dust) particles.
703 Using the libRadtran-UVSPEC radiative transfer model (RTM), driven by aerosol extinction
704 profiles measured by LiDARs at the three stations, the daily average radiative forcing (RF) of the
705 isolated volcanic plumes has been estimated with the methodology described in Sect. 2.2.2, and is
706 reported in Tab. 2. The aerosol extinction profiles used as input to the RTM are the average of the
707 observations at the core overpass time, i.e. the same period used to calculate the AOD_V in Tab.1
708 and detailed in its caption. Based on the considerations above and the complementary observations,
709 we have made the following hypotheses for non-measured optical parameters of the plumes. For
710 plume P1 at Sede Boker, a fraction of fine ash was probably present in the volcanic plume. Thus,
711 we have run the RTM using an interval of AE typical of small-sized particles (1.8-2.0) and a SSA
712 typical of partially absorbing particles (0.90-0.95). A moderately dusty background lower-
713 tropospheric atmosphere is considered for altitudes between surface to 3 km. For plume P2/W at
714 OHP, a SA-dominated plume is considered. Thus, we have run the RTM using an interval of AE
715 typical of small-sized particles (1.8-2.0) and a SSA typical of very reflective aerosols (0.95-1.00).
716 A very dusty background lower-tropospheric atmosphere is considered for altitudes between
717 surface to 5 km, based on LiDAR observations of the lowest layer of e.g. Fig. 8a-b. For plume
718 P2/E at Napoli, a fraction of ash in the volcanic plume is considered. Thus, we have run the RTM
719 using the observed AE (0.85), which is typical of larger particles than what found for P1 and P2/W,
720 and SSA typical of partly absorbing aerosols (0.90-0.95). As for plume P2/W, a very dusty
721 background lower-tropospheric atmosphere is considered for altitudes between surface to 5 km,
722 based on LiDAR observations of the lowest layer of e.g. Fig. 9a. With these assumptions, a TOA
723 RF of -0.22 ± 0.06, -0.17 ± 0.03 and -1.19 ± 0.29 W/m^2, and a surface RF of -0.66 ± 0.09, -0.21 ± 0.04

and -3.51±0.47 W/m^2 are found for P1, P2/W and P2/E, respectively. Associated with a larger AOD_V, the RF of P2/E is significantly larger than for P1 and P2/W. The surface RF is much larger than the TOA RF, for both P1 and P2/E, due to the presence of absorbing aerosols in these plumes. This means that part of the incoming shortwave radiation does not reach the surface due to the in-plume absorption, which adds to the radiation scattered back to space. For plume P2/W, the TOA and surface RF have a very similar value, which points at a very limited absorption within the plume due to the likely dominant presence of purely reflective SA. The RF values obtained for these plumes can be compared with RFs estimated in the past for proximal and distal observations of Mount Etna's emissions. Using ground LiDAR observations as input to the RTM, Sellitto et al. (2020) have estimated the RF of a typical passive degassing plume at a proximal location, about 7 km downwind Mount Etna craters and have found values of about −4.5 and −7.0 W/m^2, at TOA and surface. Mild explosions and a small fraction of ash were present during these observations. For an almost purely SA, after a dispersion of about 350 km downwind Mount Etna, Sellitto et al. (2016) have found a RF efficiency, i.e. the RF per AOD unit, of about -40 to -50 W/m^2/AOD. The RF efficiency of P2/E (about 35 W/m^2/AOD) and P1 (about 29 W/m^2/AOD) are consistent with estimations of Sellitto et al. (2020) for an ashy passive degassing plume (about 35 W/m^2/AOD). The RF efficiency of P2/W (about 47 W/m^2/AOD) is consistent with estimations of Sellitto et al. (2016) for purely SA plume. Compared with larger volcanic eruptions, our estimates are e.g. of the same order of magnitude or even larger than the impact of the Raikoke eruption in 2019 (-0.3 to -0.4 W/m^2) (Kloss et al., 2021). The Raikoke had the largest volcanic impact on the radiative balance documented in at least the last 3 years. Of course, Raikoke eruption is much more relevant than the activity of Mount Etna discussed in the present study, due to its larger scale (hemispheric) impact. This demonstrates that, even if Mount Etna eruptions are of a limited regional interest, they can have a quite relevant impact at the regional scale.

*Table 1: Summary of optical properties of volcanic plumes P1 and P2, volcanic-specific layers (V index in the table) from LiDAR observations and total-column values (T index in the table) from AERONET sun-photometric observations. *=mean value of LiDAR observations between 25/02 20:00 and 26/02 06:00; **=mean value of sun-photometric observations of 25 and 26/02; ***=mean value of sun-photometric observations of 26/02 between 05:00 and 06:00; §=mean value of LTA LiDAR observations*

753 *of 24/02 between about 19:00 and 21:30; §§=mean value of sun-photometric observations of 24/02; += mean value of LiDAR*
754 *observations of 25/02 between 17:10 and 17:40 (as in Fig. 9); ++=mean value of sun-photometric observations of 25/02*

	AOD_V (532 nm)	δ_V (532 nm)	AE_V	AOD_T (532 nm)	AE_T	SSA_T
P1: Sede Boker	$0.0076\pm0.0015^{*}$ (maximum: 0.035)	$32.3\pm1.4\%^{*}$	-	$0.099\pm0.004^{**}$ $0.116\pm0.005^{***}$	$1.16\pm0.01^{***}$	$0.88\pm0.01^{***}$
P2/W: OHP observatory	$0.0036\pm0.0014^{\S}$ (maximum: 0.0062)	-	-	$0.26\pm0.06^{\S\S}$	$0.21\pm0.10^{\S\S}$	$0.96\pm0.03^{\S\S}$
P2/E: Napoli Observatory	$0.031\pm0.006^{+}$	$10.1\pm5.8\%^{+}$	$0.85\pm0.60^{+}$	$0.310\pm0.070^{++}$	$0.92\pm0.12^{++}$	$0.94\pm0.02^{++}$

755

756 *Table 2: Summary of radiative forcing estimations of volcanic plumes P1 and P2, see text for the radiative transfer modelling*
757 *setup and hypotheses*

	TOA radiative forcing (W/m^2)	Surface radiative forcing (W/m^2)
P1: Sede Boker	-0.22 ± 0.06	-0.66 ± 0.09
P2/W: OHP observatory	-0.17 ± 0.03	-0.21 ± 0.04
P2/E: Napoli Observatory	-1.19 ± 0.29	-3.51 ± 0.47

758

759 **5 Conclusions**

760 The synergy of volcanic plumes observation and modelling at different spatio-temporal scales is
761 crucial to characterize their emission, dispersion and downwind impacts. Mount Etna experiences
762 an intense eruptive activity between February and April 2021. Within this phase, three peculiar
763 extreme events, in terms of the large SO2 emission rates (55 kt of SO2 emitted overall) and
764 injection altitude (up to 12 km), took place between 21 and 26/02, that we have studied with a
765 combination of regional-scale satellite observations and Lagrangian dispersion modelling, and
766 local downwind measurement at selected ground stations coupled with offline RTM modelling.
767 These three events and the subsequently formed plumes of volcanic effluents (plumes P1-3)
768 displayed a very uncommon dispersion towards the north, which allowed the downwind
769 observation and characterisation of the plumes due to the presence of several observatory sites in
770 this quadrant. Ground-based LiDAR observations and complementary information from
771 observations and modelling at the sites of Sede Boker, Israel (plume P1), OHP (western end of
772 plume P2 – P2/W) and Napoli (eastern end of plume P2 – P2/E) revealed a complex inter- (P1
773 versus P2) and intra-plume (P2/W versus P2/E) variability of the morphology, composition, optical
774 properties and radiative impacts of Mount Etna plumes. Plume P1 has been detected at about 10
775 then descending to 5-6 km after only 4-5 days atmospheric aging, with depolarisation ratio
776 consistent with a possible presence of in-plume ash. Plume P2 displayed a dramatic variability
777 from east to west ends, with a thin and likely SA-dominated plume to the west and a dense and
778 likely ash-bearing plume to the east. Both the AOD (0.004 to 0.03) and local clear-sky daily

779 average shortwave radiative forcing (-0.2 to -1.2 W/m^2, at TOA and -0.2 to -3.5 W/m^2 at the
780 surface) point at a very relevant impact on the upper-tropospheric aerosol layer and the regional
781 climate at the continental scale, in the Mediterranean. In addition, the synergy of observations and
782 modelling presented in the present work allowed to empirically disentangle the information about
783 volcanic aerosols and other aerosol sources, like mineral dust.

784 **Acknowledgments, Samples, and Data**

785 This work has been funded by: CNES (Centre National d'Études Spatiales) via TOSCA/IASI
786 grant; CNRS (Centre national de la recherche scientifique)-INSU(Institut National des Sciences
787 de l'Univers) PNTS (Programme National de Télédétection Spatiale) via MIA-SO2 grant. This
788 work benefited from the support of the ACTRIS-Fr Infrastructure and ENSG (Ecole Nationale des
789 Sciences Géographiques) at the OHP site. Stefano Corradini, Luca Merucci, Daniele Stelitano and
790 Lorenzo Guerrieri work was supported by the ESA project VISTA (Volcanic monItoring using
791 SenTinel sensors by an integrated Approach), grant number 4000128399/19/I-DT and by the
792 INGV project IMPACT. IASI is a joint mission of EUMETSAT and the Centre National d'Etudes
793 Spatiales (CNES, France). The authors acknowledge the AERIS data infrastructure for providing
794 access to the IASI SO2, and IASI Level 1c and AVHRR-CLARA2 data, inputs to the AEROIASI
795 algorithms. The authors acknowledge ULB-LATMOS for the development of the IASI SO2
796 retrieval algorithm. The ECMWF is acknowledged for providing the meteorological analyses used
797 for both AEROIASI observations and the FLEXPART simulations. The authors thank Pierre-Eric
798 Blanc and Baptiste Camus for their technical support on the OHP GAIA system. They are grateful
799 to Philippe Goloub and Ioana Popovici at Laboratoire Optique de Lille for their advices regarding
800 the treatment of the GAIA datasets. The PIs of the PHOTON-AERONET stations of OHP
801 (Philippe Goloub and Thierry Podvin), Napoli (Nicola Spinelli) and Sede Boker (Arnold Karnieli)
802 are gratefully acknowledged.

803 **References**

804 Ancellet G. and Beekmann M. (1997) Evidence for changes in the ozone concentrations in the
805 free troposphere over southern France from 1976 to 1995, Atmospheric Environment, 31, 17,
806 2835-2851, https://doi.org/10.1016/S1352-2310(97)00032-0.
807 Andersson, S., Martinsson, B., Vernier, JP. et al. (2015) Significant radiative impact of volcanic
808 aerosol in the lowermost stratosphere. Nat. Commun. 6, 7692.
809 doi:https://doi.org/10.1038/ncomms8692

810 Ansmann, A., Riebesell, M., and Weitkamp, C. (1990) Measurement of atmospheric aerosol
811 extinction profiles with a Raman lidar. Opt. Lett., 15, 746–748.doi:10.1364/OL.15.000746.

812 Biele, J., Beyerle, G., and Baumgarten, G. (2000) Polarization lidar: corrections of instrumental
813 effects. Opt. Express, 7,427–435, doi:10.1364/OE.7.000427.

814 Biermann, U.M., Luo, B.P., Peter, T. (2000) Absorption Spectra and Optical Constants of Binary
815 and Ternary Solutions of H2SO4, HNO3, and H2O in the Mid Infrared at Atmospheric
816 Temperatures. J. Phys. Chem. A, 104, 783–793.

817 Bilal, M.; Nazeer, M.; Nichol, J.; Qiu, Z.; Wang, L.; Bleiweiss, M.P.; Shen, X.; Campbell, J.R.;
818 Lolli, S. Evaluation of Terra-MODIS C6 and C6.1 Aerosol Products against Beijing, XiangHe,
819 and Xinglong AERONET Sites in China during 2004-2014. Remote Sens. 2019, 11, 486.
820 https://doi.org/10.3390/rs11050486.

821 Boselli, A., D'Emilio, M., Sannino, A., Wang, X., and Amoruso, S. (2021) Remote sensing and
822 near surface observations of aerosol properties measured in real time during a big fire event on
823 Mount Vesuvius, Remote Sensing, 13(10), https://doi.org/10.3390/rs13102001.

824 Campbell, J.R. J.R., D.L. Hlavka, E.J. Welton, C.J. Flynn, D.D. Turner, J.D. Spinhirne, V.S.
825 Scott, and I.H. Hwang, 2002. Full-time, Eye-Safe Cloud and Aerosol Lidar Observation at
826 Atmospheric Radiation Measurement Program Sites: Instrument and Data Processing, J. Atmos.
827 Oceanic Technol., 19, 431-442.

828 Campbell, J. R., Dolinar, E. K., Lolli, S., Fochesatto, G. J., Gu, Y., Lewis, J. R., ... & Welton, E.
829 J. (2021). Cirrus cloud top-of-the-atmosphere net daytime forcing in the Alaskan subarctic from
830 ground-based MPLNET monitoring. Journal of Applied Meteorology and Climatology, 60(1),
831 51-63.

832 Clarisse, L., Hurtmans, D., Clerbaux, C., Hadji-Lazaro, J., Ngadi, Y., and Coheur, P.-F. (2012)
833 Retrieval of sulphur dioxide from the infrared atmospheric sounding interferometer (IASI),
834 Atmos. Meas. Tech., 5, 581–594, https://doi.org/10.5194/amt-5-581-2012.

835 Clarisse, L., Coheur, P.-F., Theys, N., Hurtmans, D., and Clerbaux, C. (2014) The 2011 Nabro
836 eruption, a SO2 plume height analysis using IASI measurements, Atmos. Chem. Phys., 14,
837 3095–3111, https://doi.org/10.5194/acp-14-3095-2014.

838 Clerbaux, C., Boynard, A., Clarisse, L., George, M., Hadji-Lazaro, J., Herbin, H., Hurtmans, D.,
839 Pommier, M., Razavi, A., Turquety, S., et al. (2009) Monitoring of atmospheric composition
840 using the thermal infrared IASI/MetOp sounder. Atmos. Chem. Phys., 9, 6041–6054.

841 Corradini S.; Guerrieri L.; Lombardo V.; Merucci L.; Musacchio M., Prestifilippo M.; Scollo S.;
842 Silvestri M.; Spata G.; Stelitano D. (2018) Proximal monitoring of the 2011-2015 Etna lava
843 fountains using MSG-SEVIRI data. *MDPI Geosciences*, 8, 140;
844 doi:10.3390/geosciences8040140

845 Corradini S., Guerrieri L., Stelitano D., Salerno G., Scollo S., Merucci L., Prestifilippo M.,
846 Musacchio M., Silvestri M., Lombardo V., Caltabiano T. (2020) Near Real-Time Monitoring of
847 the Christmas 2018 Etna Eruption Using SEVIRI and Products Validation, Remote Sens., 12,
848 1336; doi:10.3390/rs12081336.

849 Corradini S., Guerrieri L., Brenot H., Clarisse L., Merucci L., Pardini F., Prata A.J., Realmuto
850 V.J., Stelitano D., Theys N. (2021) Tropospheric Volcanic SO2 Mass and Flux Retrievals from
851 Satellite. The Etna December 2018 Eruption", Remote Sens., 13, 2225.
852 https://doi.org/10.3390/rs13112225.

853 Cuesta, J., Eremenko, M., Flamant, C., Dufour, G., Laurent, B., Bergametti, G., Höpfner, M.,
854 Orphal, J., Zhou, D. (2015) Three-dimensional distribution of a major desert dust outbreak over
855 East Asia in March 2008 derived from IASI satellite observations. J. Geophys. Res. Atmos., 120,
856 7099–7127.

857 Cuesta, J., Flamant, C., Gaetani, M., et al. (2020) Three-dimensional pathways of dust over the
858 Sahara during summer 2011 as revealed by new Infrared Atmospheric Sounding Interferometer
859 observations. Q J R Meteorol Soc.; 146: 2731– 2755. https://doi.org/10.1002/qj.3814

860 Di Biagio, C., Formenti, P., Balkanski, Y., Caponi, L., Cazaunau, M., Pangui, E., Journet, E.,
861 Nowak, S., Caquineau, S., Andreae, M. O., Kandler, K., Saeed, T., Piketh, S., Seibert, D.,
862 Williams, E., and Doussin, J.-F. (2017) Global scale variability of the mineral dust long-wave

refractive index: a new dataset of in situ measurements for climate modeling and remote sensing, Atmos. Chem. Phys., 17, 1901–1929, https://doi.org/10.5194/acp-17-1901-2017.

M. Dittman et al. (2002), Nadir ultraviolet imaging spectrometer for the NPOESS Ozone Mapping and Profiler Suite (OMPS), Proc. SPIE, 4814.

Emde, C., Buras-Schnell, R., Kylling, A., Mayer, B., Gasteiger, J., Hamann, U., Kylling, J., Richter, B., Pause, C., Dowling, T., and Bugliaro, L. (2016) The libRadtran software package for radiative transfer calculations (version 2.0.1), Geosci. Model Dev., 9, 1647–1672, https://doi.org/10.5194/gmd-9-1647-2016.

Fernald, F. G. "Analysis of atmospheric lidar observations: some comments." Applied optics 23.5, 1984: 652-653.

Freudenthaler,V., Esselborn, M., Wiegner, M., Heese, B., Tesche, M., and Ansmann, A. (2009) Depolarization ratio profiling at several wavelengths in pure Saharan dust during SAMUM 2006. Tellus 2009, 61B, 165–179. Doi: 10.1111/j.16000889.2008.00396.x.

Gaudel A., Ancellet G., Godin-Beekmann S. (2015) Analysis of 20 years of tropospheric ozone vertical profiles by lidar and ECC at Observatoire de Haute Provence (OHP) at 44°N, 6.7°E, Atmospheric Environment, 113, 78-89, https://doi.org/10.1016/j.atmosenv.2015.04.028.

Guermazi, H., Sellitto, P., Cuesta, J., Eremenko, M., Lachatre, M., Mailler, S., Carboni, E., Salerno, G., Caltabiano, T., Menut, L., Serbaji, M.M., Rekhiss, F., Legras, B. (2021) Quantitative Retrieval of Volcanic Sulphate Aerosols from IASI Observations. Remote Sens., 13, 1808. https://doi.org/10.3390/rs13091808

Guerrieri, L., Merucci, L., Corradini, S., Pugnaghi, S. (2015) Evolution of the 2011 Mt. Etna ash and SO2 lava fountain episodes using SEVIRI data and VPR retrieval approach. J. Volcanol. Geotherm. Res., 291, 63–71.

Haywood, J. M., Jones, A., Clarisse, L., Bourassa, A., Barnes, J., Telford, P. et al. (2010), Observations of the eruption of the Sarychev volcano and simulations using the HadGEM2 climate model, *Journal of Geophysical Research, 115*, D21212, doi:10.1029/2010JD014447.

Holben, B.; Eck, T.; Slutsker, I.; Tanré, D.; Buis, J.; Setzer, A.; Vermote, E.; Reagan, J.; Kaufman, Y.; Nakajima, T.; et al. (1998) AERONET—A Federated Instrument Network and Data Archive for Aerosol Characterization. Remote Sens. Environ., 66, 1–16.

Hoshyariapour, A. (2021) February 2021: A dusty month for Europe https://blogs.egu.eu/divisions/as/2021/04/03/february-2021-a-dusty-month-for-europe/

Khaykin, S. M et al. (2017) Variability and evolution of the midlatitude stratospheric aerosol budget from 22 years of ground-based lidar and satellite observations, Atmos. Chem. Phys., 17, 1829–1845, https://doi.org/10.5194/acp-17-1829-2017.

Kearney, C.S.; Watson, I.M. (2009) Correcting satellite-based infrared sulfur dioxide retrievals for the presence of silicate ash., J. Geophys. Res. Space Phys., 114, 22208.

Keckhut P., Hauchecorne A., and Chanin, M.L. (1993) A critical review on the data base acquired for the long term surveillance of the middle atmosphere by French Rayleigh lidars, J. Atmos. Oceanic Technol., 10, 850-867.

902 Lewis, J.R., J.R. Campbell, E.J. Welton, S.A. Stewart, and P.C. Haftings (2016). Overview of
903 MPLNET Version 3 Cloud Detection. J. Atmos. Oceanic Tech., 33, 2113 – 2134, doi:
904 10.1175/JTECH-D-15-0190.1.

905 Lolli, S.; D'Adderio, L.; Campbell, J.; Sicard, M.; Welton, E.; Binci, A.; Rea, A.; Tokay, A.;
906 Comerón, A.; Baldasano, R.B.J.M.; et al. Vertically Resolved Precipitation Intensity Retrieved
907 through a Synergy between the Ground-Based NASA MPLNET Lidar Network Measurements,
908 Surface Disdrometer Datasets and an Analytical Model Solution. Remote Sens. 2018, 10, 1102

909 Lolli, S.; Vivone, G.; Lewis, J.R.; Sicard, M.; Welton, E.J.; Campbell, J.R.; Comerón, A.;
910 D'Adderio, L.P.; Tokay, A.; Giunta, A.; Pappalardo, G. Overview of the New Version 3 NASA
911 Micro-Pulse Lidar Network (MPLNET) Automatic Precipitation Detection Algorithm. Remote
912 Sens. 2020, 12, 71. https://doi.org/10.3390/rs12010071

913 Klett JD. Stable analytical inversion solution for processing lidar returns. Appl Opt. 1981 Jan
914 15;20(2):211-20. doi: 10.1364/AO.20.000211. PMID: 20309093.

915 Kloss, C., Berthet, G., Sellitto, P., Ploeger, F., Taha, G., Tidiga, M. et al. (2021). Stratospheric
916 aerosol layer perturbation caused by the 2019 Raikoke and Ulawun eruptions and their radiative
917 forcing, *Atmospheric Chemistry and Physics, 21*, 535–560, https://doi.org/10.5194/acp-21-535-
918 2021.

919 Krotkov, N. A., Krueger, A. J. & Bhartia, P. K. (1997). Ultraviolet optical model of volcanic
920 clouds for remote sensing of ash and sulfur dioxide. *Journal of Geophysical Research:*
921 *Atmospheres, 102*, 21891–21904. https://doi.org/10.1029/97JD01690.

922 Malavelle, F. F., Haywood, J. M., Jones, A., Gettelman, A., Clarisse, L., Bauduin, S. et al. (2017)
923 Strong constraints on aerosol–cloud interactions from volcanic eruptions. *Nature, 546*, 485–491.

924 Merucci, L.; Burton, M.; Corradini, S.; Salerno, G. (2011) Reconstruction of SO2 flux emission
925 chronology from space-based measurements. *J. Volcanol. Geotherm. Res.,* 206, 80–87.
926 doi:10.1016/j.jvolgeores.2011.07.002.

927 Michaud, J., Krupitsky, D., Grove, J. & Anderson, B. (2005). Volcano related atmospheric
928 toxicants in Hilo and Hawaii Volcanoes National Park: Implications for human health.
929 *Neurotoxicology, 26*, 555–563. https://doi.org/10.1016/j.neuro.2004.12.004.

930 Oppenheimer, C., Scaillet, B., & Martin, R. S. (2011). Sulfur Degassing From Volcanoes:
931 Source Conditions, Surveillance, Plume Chemistry and Earth System Impacts, *Reviews in*
932 *Mineralogy and Geochemistry, 72*, 363–421, doi:10.2138/rmg.2011.73.13, 2011.

933 Pisso, I. et al. (2019) The Lagrangian particle dispersion model FLEXPART version 10.4,
934 Geosci. Model Dev., 12, 4955–4997, https://doi.org/10.5194/gmd-12-4955-2019.

935 Prata, A. T., Young, S. A., Siems, S. T., & Manton, M. J. (2017). Lidar ratios of stratospheric
936 volcanic ash and sulfate aerosols retrieved from CALIOP measurements. Atmospheric
937 Chemistry and Physics, 17(13), 8599-8618.

938 Ridley, D. A., Solomon S., Barnes, J. E., Burlakov, V. D., Deshler, T., Dolgii, S. I. et al. (2014),
939 Total volcanic stratospheric aerosol optical depths and implications for global climate change,
940 *Geophysical Research Letters, 41*, 7763– 7769, doi:10.1002/2014GL061541.

941 Santer, B. D., Bonfils, C., Painter, J. F., Zelinka, M. D., Mears, C., Solomon, S. et al. (2014).
942 Volcanic contribution to decadal changes in tropospheric temperature. *Nature Geoscience, 7*,
943 185–189.

944 Scollo, S.; Prestifilippo, M.; Spata, G.; D'Agostino, M., Coltelli, M. (2009) Monitoring and
945 forecasting Etna volcanic plumes. Nat. Hazards Earth Syst. Sci., 9, 1573–1585.

946 Sellitto, P. & Briole, P. (2015). On the radiative forcing of volcanic plumes: Modelling the
947 impact of Mount Etna in the Mediterranean. *Annals of Geophysics, 58*.
948 https://doi.org/10.4401/ag-6879 (2015).

949 Sellitto, P., di Sarra, A., Corradini, S., Boichu, M., Herbin, H., Dubuisson, P., et al. (2016).
950 Synergistic use of Lagrangian dispersion and radiative transfer modelling with satellite and
951 surface remote sensing measurements for the investigation of volcanic plumes: the Mount Etna
952 eruption of 25–27 October 2013, *Atmospheric Chemistry and Physics, 16*, 6841–6861,
953 https://doi.org/10.5194/acp-16-6841-2016.

954 Sellitto, P., Zanetel, C., di Sarra, A., Salerno, G., Tapparo, A. et al. (2017a) The impact of Mount
955 Etna sulfur emissions on the atmospheric composition and aerosol properties in the central
956 Mediterranean: A statistical analysis over the period 2000–2013 based on observations and
957 Lagrangian modelling. *Atmospheric Environment, 148*, 77–88.
958 https://doi.org/10.1016/j.atmosenv.2016.10.032.

959 Sellitto, P., Salerno, G., La Spina, A., Caltabiano, T., Scollo, S., Boselli, A. et al. (2020). Small-
960 scale volcanic aerosols variability, processes and direct radiative impact at Mount Etna during
961 the EPL-RADIO campaigns. *Scientific Reports, 10*, 15224. https://doi.org/10.1038/s41598-020-
962 71635-1

963 Stelitano D., Corradini S., Merucci L., Guerrieri L. (2020) Procedure automatiche per la
964 rilevazione e la stima dei parametri delle nubi vulcaniche da satellite, MISCELLANEA INGV,
965 Progetto "Sale Operative Integrate e Reti di monitoraggio del futuro: l'INGV 2.0". Report finale,
966 ISSN 1590-2595, 57. https://doi.org/10.13127/misc/57/20

967 Stevenson, D. S., Johnson, C. E., Collins, W. J. & Derwent, R. G. (2003). The tropospheric
968 sulphur cycle and the role of volcanic SO2. *Geological Society of London Special Publication,*
969 *213*, 295–305. https://doi.org/10.1144/GSL.SP.2003.213.01.18.

970 Stiller, G. The Karlsruhe Optimized and Precise Radiative Transfer Algorithm (KOPRA) (2000)
971 Wissenschaftliche Berichte, FZKA; Forschungszentrum Karlsruhe: Karlsruhe, Germany, 2000.

972 Theys,N., I. De Smedt, H. Yu, T. Danckaert, J. van Gent,C. Hörmann, T. Wagner, P. Hedelt, H.
973 Bauer, F. Romahn, M. Pedergnana, D. Loyola, M. Van Roozendael (2017) Sulfur dioxide
974 operational retrievals from TROPOMI onboard Sentinel-5 Precursor: Algorithm Theoretical
975 Basis, Atmos. Meas. Tech., 10, 119-153, doi:10.5194/amt-10-119-2017.

976 Veefkind, J.P., Aben, I., McMullan, K., Förster, H., De Vries, J., Otter, G., Claas, J.,
977 Eskes, H.J., De Haan, J.F., Kleipool, Q., Van Weele, M., Hasekamp, O., Hoogeveen, R.,
978 Landgraf, J., Snel, R., Tol, P., Ingmann, P., Voors, R., Kruizinga, B., Vink, R., Visser, H., and
979 Levelt, P.F. (2012). TROPOMI on the ESA Sentinel-5 Precursor: A GMES mission for
980 global observations of the atmospheric composition for climate, air quality and ozone
981 layer applications. Remote Sensing of Environment, 120: 70–83.
982 doi:10.1016/j.rse.2011.09.027

983 von Glasow, R., Bobrowski, N. & Kern, C. (2009), The effects of volcanic eruptions on the
984 atmospheric chemistry. *Chemical Geology, 263*, 131–142.
985 https://doi.org/10.1016/j.chemgeo.2008.08.020.

986 Wandinger, U., Nicolae, D., Pappalardo, G., Mona, L., Comerón, A. (2020) ACTRIS and its
987 aerosol remote sensing component, EPJ Web Conferences 237, 05003,
988 https://doi.org/10.1051/epjconf/202023705003.

989 Webley, P. W., Steensen, T., Stuefer, M., Grell, G., Freitas, S., & Pavolonis, M. (2012).
990 Analyzing the Eyjafjallajökull 2010 eruption using satellite remote sensing, lidar and WRF-
991 Chem dispersion and tracking model, *Journal of Geophysical Research: Atmospheres, 117*,
992 D00U26, doi:10.1029/2011JD016817.

993 Welton, E.J. K.J. Voss, H.R. Gordon, H. Maring, A. Smirnov, B. Holben, B. Schmid, J.M.
994 Livingston, P.B. Russell, P.A. Durkee, P. Formenti, M.O. Andreae (2000). Ground-based Lidar
995 Measurements of Aerosols During ACE-2: Instrument Description, Results, and Comparisons
996 with other Ground-based and Airborne Measurements, Tellus B, 52, 635-650.

997 Welton, E.J.; Campbell, J.R.; Spinhirne, J.D.; Stanley Scott, V., III. (2001). Global monitoring of
998 clouds and aerosols using a network of micropulse lidar systems. SPIE Conf. Proc., 4153, 151–
999 158

1000 Welton, E.J., S.A. Stewart, J.R. Lewis, L.R. Belcher, J.R. Campbell, and S. Lolli (2018). Status
1001 of the NASA Micro Pulse Lidar Network (MPLNET): Overview of the network and future plans,
1002 new Version 3 data products, and the polarized MPL. EPJ Web of Conferences, 176,
1003 https://doi.org/10.1051/epjconf/201817609003.

1004 Wielicki, B.A., Cess, R.D., King, M.D., Randall, D.A., Harrison, E.F (1995) Mission to planet
1005 Earth: Role of clouds and radiation in climate. Bull. Am. Meteorol. Soc., 76, 2125–2154

1006 Winker, D.M., Pelon, J., Coakley, J.A., Ackerman, S.A., Charlson, R.J., Colarco, P.R., Flamant,
1007 P., Fu, Q., Hoff, R.M., Kittaka, C. et al. (2010) The CALIPSO Mission. Bull. Am. Meteorol.
1008 Soc. 91, 1211–1230.

1009 **Supplementary Information**

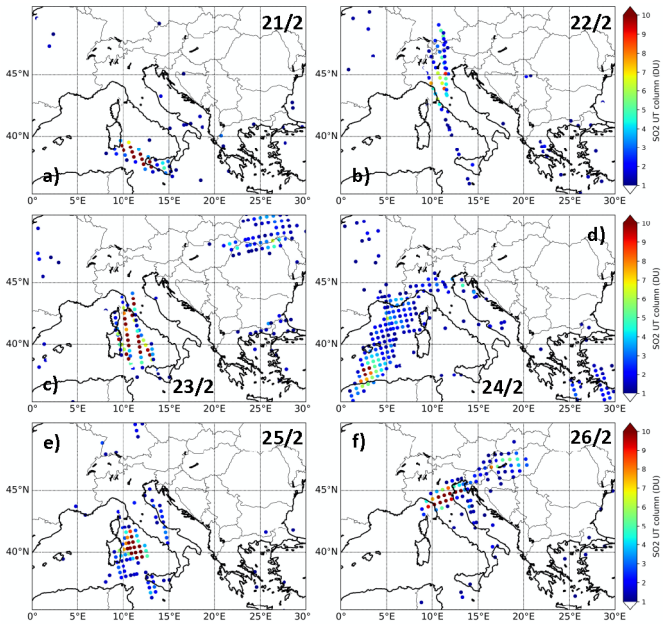

1010
1011 *Supplementary Figure 1: OMPS-NM upper-tropospheric SO2 observations from 21 (panel a) to 26/02/2021 (panel f).*

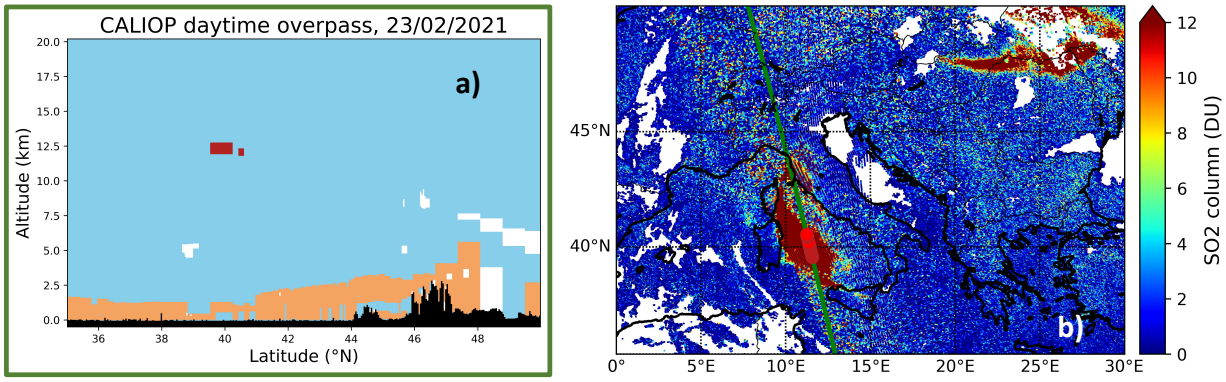

1012
1013 *Supplementary Figure 2: (a) Feature layer classification (same color code as in Fig. 6) for CALIOP daytime overpass, at ~1:30*
1014 *pm, for 23/02/2021. (b) Sentinel-5p TROPOMI SO2 column observations for 23/02/2021. The green line in panel b is the ground*
1015 *track of CALIOP observations of panel a. The position of the stratospheric aerosol (volcanic) feature, identified in panel a, is*
1016 *also indicated in panel b as red circles.*

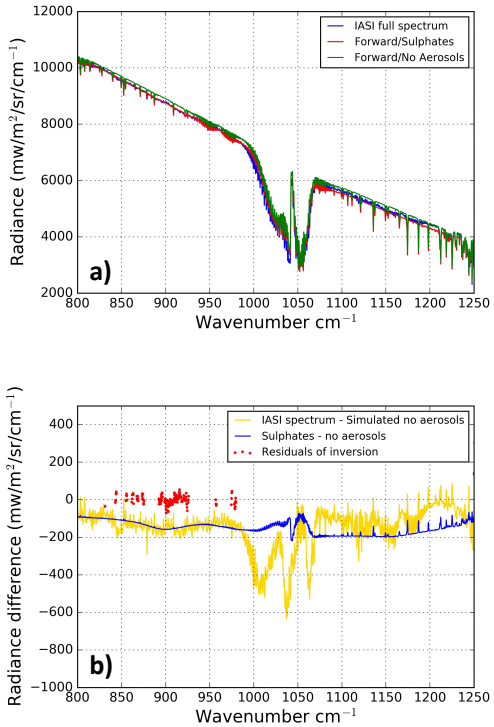

Supplementary Figure 3: The IASI spectrum (blue) taken at OHP (longitude: 5.74°E, latitude: 43.93°N) observed during daytime IASI overpass on 24/02/2021, the AEROIASI-H2SO4 fitted spectrum (red) and a fitted spectrum without SA (green). Spectral radiance differences of the IASI observed spectrum and the fitted spectrum without SA (yellow), the fitted spectra with and without SA (blue) and the fitting residuals (red dots). The SA size distribution is a log-normal with 0.5 μm mean size and 0.5 standard deviation. A mixing ratio of the sulphuric acid of 57% has been considered. The observed spectral signature of SA is observed in the range 800-950 cm^{-1}. For more details please refer to Guermazi et al. (2021). The thermal infrared SA-specific AOD retrieval for this observation is 0.05.